Biophysical Journal Volume 107 November 2014 2164–2176

Article

Understanding Nucleotide-Regulated FtsZ Filament Dynamics and the Monomer Assembly Switch with Large-Scale Atomistic Simulations

Erney Ramírez-Aportela,[1,2] José Ramón López-Blanco,[1] José Manuel Andreu,[2] and Pablo Chacón[1,*]
[1]Department of Biological Physical Chemistry, Instituto de Química-Física Rocasolano, CSIC, Madrid, Spain; and [2]Department of Chemical and Physical Biology, Centro de Investigaciones Biológicas, CSIC, Madrid, Spain

ABSTRACT Bacterial cytoskeletal protein FtsZ assembles in a head-to-tail manner, forming dynamic filaments that are essential for cell division. Here, we study their dynamics using unbiased atomistic molecular simulations from representative filament crystal structures. In agreement with experimental data, we find different filament curvatures that are supported by a nucleotide-regulated hinge motion between consecutive FtsZ monomers. Whereas GTP-FtsZ filaments bend and twist in a preferred orientation, thereby burying the nucleotide, the differently curved GDP-FtsZ filaments exhibit a heterogeneous distribution of open and closed interfaces between monomers. We identify a coordinated Mg^{2+} ion as the key structural element in closing the nucleotide site and stabilizing GTP filaments, whereas the loss of the contacts with loop T7 from the next monomer in GDP filaments leads to open interfaces that are more prone to depolymerization. We monitored the FtsZ monomer assembly switch, which involves opening/closing of the cleft between the C-terminal domain and the H7 helix, and observed the relaxation of isolated and filament minus-end monomers into the closed-cleft inactive conformation. This result validates the proposed switch between the low-affinity monomeric closed-cleft conformation and the active open-cleft FtsZ conformation within filaments. Finally, we observed how the antibiotic PC190723 suppresses the disassembly switch and allosterically induces closure of the intermonomer interfaces, thus stabilizing the filament. Our studies provide detailed structural and dynamic insights into modulation of both the intrinsic curvature of the FtsZ filaments and the molecular switch coupled to the high-affinity end-wise association of FtsZ monomers.

INTRODUCTION

The cytoskeletal protein FtsZ forms filaments that organize into the bacterial Z-ring, which recruits other cell-division proteins and may lead to membrane constriction (2) through a combination of FtsZ filament condensation, bending, and recycling. FtsZ polymers attached to engineered membranes exhibit an intrinsic curvature and twist, which have been suggested to facilitate their equatorial assembly in the cell (3). FtsZ polymers attached via the partner protein FtsA to a supported membrane organize into dynamic patterns driven by the treadmilling and fragmentation of polar FtsZ filaments in the absence of motor proteins (4). FtsZ and its eukaryotic relative tubulin are GTPases that form similar protofilaments with GTP at the interfaces between consecutive monomers (5), and both have built-in molecular switches that are triggered by nucleotide γ-phosphate hydrolysis and permit assembly-disassembly regulation. Thus, GTP binding displaces the balance toward the formation of FtsZ filaments, sheets, and bundle condensates, whereas upon hydrolysis to GDP, FtsZ filaments curve and eventually depolymerize.

Given its ubiquity and its central role in bacterial cell division, FtsZ is an attractive target for the development of new antibiotics (6). FtsZ has been validated as the target of the in vivo effective antibacterial compound PC190723 (7), which modulates FtsZ assembly by stabilizing its polymers (8,9) and binds into the cleft between the C-terminal domain and the core helix H7 of this protein (9–11). Moreover, several nucleotide analogs (12,13) and nonnucleotide compounds that selectively target the nucleotide site of FtsZ have also been identified (14–16).

To explain the puzzlingly cooperative assembly behavior of single-stranded FtsZ protofilaments, a self-switching model between inactive and actively associating protein conformers has been proposed to be responsible for transmitting the assembly conformational changes from one FtsZ monomer to another along the filament (17–19). In a previous work (20), we predicted that the FtsZ assembly switch involves an interdomain movement that closes and opens the cleft between the C-terminal domain and the core helix H7, thereby modifying the axial association between FtsZ monomers. Interestingly, mutations that block FtsZ in its inactive closed conformation and mutations that are resistant to PC190732 (7) have both been found to cluster at the interdomain cleft, indicating that the FtsZ switch is targeted (20). This molecular switch has also been supported by the changes observed in the tryptophan-induced quenching of a fluorophore after FtsZ assembly (21). However, all reported crystallographic structures

Submitted June 27, 2014, and accepted for publication September 30, 2014.
*Correspondence: pablo@chaconlab.org
Editor: David Sept.

0006-3495/14/11/2164/13 $2.00
http://dx.doi.org/10.1016/j.bpj.2014.09.033

of FtsZ from various organisms have exhibited a closed-cleft conformation (22), with the exception of the recent *Staphylococcus aureus* FtsZ (SaFtsZ) structure, in which the crystal packing exhibited a straight filament formed by open-cleft monomers (9–11). This open-cleft structure has been considered to be functionally relevant because 1), it facilitates the formation of a tight interface that encloses the nucleotide between bacterial FtsZ monomers in the filament, in contrast to the accessible nucleotide in the more open association interface of an archaeal FtsZ dimer (23); and 2), it permits the binding of PC190723 as a wedge into the open interdomain cleft, which explains the stabilizing effect of this ligand on FtsZ assembly. A structural comparison of SaFtsZ with other FtsZs supports the cleft-opening mechanism of the FtsZ assembly switch. However, proof involving the same FtsZ protein, such as a closed-cleft monomeric structure of the same Sa-FtsZ molecule or an open filamentous structure of other FtsZs, is required. Nevertheless, the open-cleft Sa-FtsZ filament structure constitutes an ideal framework in which to study FtsZ assembly dynamics. Previous molecular-dynamics (MD) studies have focused on monomeric or dimeric crystallographic structures of archaeal or mycobacterial FtsZ in the inactive closed-cleft conformation (24–29). Although these studies shed light on several aspects of FtsZ dynamics, they were not based on the functional open-cleft FtsZ structure, or their filament simulations were not sufficiently long. Here, we describe extensive MD simulations of bacterial SaFtsZ filaments from more realistic crystallographic FtsZ filament structures (10,11). As we will show, the results of these simulations allow for a better understanding of nucleotide-dependent filament dynamics, provide atomic insight into how nucleotide hydrolysis weakens the association between monomers along the filament, and unravel the mechanism of the SaFtsZ assembly switch that is blocked by PC190723 to inhibit bacterial cell division.

MATERIALS AND METHODS

We studied the dynamic properties of FtsZ filament structures in three different states: with bound GTP, with GDP, and with GDP plus PC190723 (hereafter abbreviated as PC). MD simulations were performed on FtsZ heptamers (~500,000 atoms, including water molecules) with GROMACS version 4.6 (30,31) using the Amber99sb (32) force field. In each case, independent MD simulations of 300 ns duration were performed twice to confirm the reproducibility of the results. In the case of the most flexible filament, the GDP-bound one, we extended the simulation to 500 ns. The filament length was sufficient to sample different representative conformations of the FtsZ filaments. The heptameric filament had the largest affordable size to perform long-scale MD simulations in our available supercomputing facilities. The filament's stability and the consistent dynamical behavior of the monomer interfaces found in our simulations provide enough confidence that our observations grasp the main features of FtsZ filament dynamics, although inaccessible larger-sized filaments (on the order of 100 monomers) and longer timescales (several microseconds) should better reproduce the macroscopic mechanics of FtsZ filaments. Note that we carefully removed the influence of end monomers in the dynamic measurements to avoid border effects. We observed consistent results in all simulations that were quite stable after 200 ns. In all cases, the simulations reached a steady state and the integrity of the filaments was well maintained over the long simulation times (see Fig. S1 in the Supporting Material). We also performed simulations of isolated SaFtsZ monomers bound to GDP, GTP, and GDP + PC using the same simulation parameters employed for the filaments.

Systems preparation

The initial straight coordinates were obtained from the x-ray crystal structures of SaFtsZ (11) bound to GDP (PDB ID 3V08) and to complex PC190723 (PDB ID 3V0B). The GTP filament was obtained by replacing the GDP coordinates of the GDP filament with GTP and Mg^{2+}, acquired from the *Methanococcus jannaschhi* FtsZ (MjFtsZ) atomic structure (23) (PDB ID 1W5A). Filaments of seven monomers were generated by crystallographic symmetry operations. The parameters of the ligands GDP and GTP were taken from the Amber parameter database. The topology of PC190723 was constructed using the AmberTools utilities of the AMBER11 package (33). The generalized AMBER force field (34) was chosen to parametrize the molecule. Ab initio quantum mechanics calculations at the HF/6-31+G* level were performed, and the restrained electrostatic potential method was used to assign partial charges to these molecules.

The filament structures were placed in triclinic boxes of explicit TIP3P water molecules (35) with a minimum distance of 15 Å between the protein surface and the border of the box. The boxes were replicated by periodic boundary conditions. Water molecules were replaced with sodium counterions to neutralize the systems. Additional sodium and chloride ions were added corresponding to an ionic strength of 50 mM. Extra Mg^{2+} and Cl^{-} ions were also added to obtain a concentration of 10 mM, which corresponds to experimental FtsZ filament assembly conditions.

MD simulations

For each system, two independent simulations with different initial velocities were performed using the parameters described below. The solvated systems were minimized using steepest descent followed by conjugate gradient methods (double precision). Initial velocities were randomly assigned according to a Maxwell distribution at 50 K in accordance with the atomic masses. To equilibrate water and ions around the filaments, each system was gradually heated over 6 ns from 50 to 298 K by increasing the temperature by 50 K every 1 ns. Heating was carried out with position restraints on the protein and ligands atoms. After that, the position restraint was limited to backbone atoms only and equilibration was continued for another 6 ns. During the equilibration, a 2 fs integration time step was used and the neighbor list was updated every 10th time step. Finally, the position restraints were removed and the equilibrated filament structures were used as the starting points for 300 ns and 500 ns production MD simulations. An integration time step of 2 fs was used. The trajectories were sampled every 40 ps for analysis. Simulations were carried out in the NPT ensemble. The pressure of the simulation boxes was kept at an average of 1 bar using the Berendsen barostat (36) with a time constant of 0.5 ps and a compressibility of 4.5×10^{-5} bar^{-1}. The solvent and filament-ligand complex were coupled separately to an external heat bath at 298 K with the velocity-rescaling thermostat (37) using a time constant of 0.1 ps. The LINCS algorithm (38) was used to constrain the bond lengths, and the water geometries were constrained by the SETTLE algorithm (39). The electrostatic interactions were evaluated using the particle-mesh Ewald method (40) with van der Waals interactions truncated at 14 Å.

To study the effect of Ca^{2+}, we repeated the MD simulations of the GDP and PC filaments while including this bound cation, as in the original crystallographic structures. We performed additional MD simulations of the GDP filament by substituting Na^{+} with K^{+}. No significant difference was observed with respect to the monovalent cation used.

RESULTS

Dynamics of bacterial FtsZ filaments

The initial states of the MD trajectories had the same straight nature of the crystallographic filaments, which was rapidly lost in all cases, revealing the intrinsic flexibility of FtsZ filaments. The GDP filament exhibited a higher conformational variability, whereas the GTP and PC filaments adopted more rigidly curved conformations. These dynamical differences are illustrated in Fig. 1 *A*, where the final snapshot of each filament (*yellow ribbons*) is superimposed on an illustrative snapshot acquired during the previous 100 ns (*gray*). The nucleotide-dependent curvatures can be directly visualized in Movie S1, which displays the entire trajectories in parallel. It is apparent that the fluctuation around the curved pattern was very small for the PC filament, slightly larger for the GTP filament, and very large for the GDP case. In the GTP-bound filament, the nucleotide γ phosphate and the coordinated Mg^{2+} ion induced filament curvature in a preferred orientation (Fig. 1 *A*), in which the association interfaces are closed (Fig. 1 *B*). The GDP-bound filament exhibited various curved patterns and even adopted S-shaped conformations (Fig. 1 *A*) by opening and closing the association interfaces between the monomers. From the illustrative dimer interfaces displayed in Fig. 1 *B*, it is readily apparent how the GDP-open interface (in *green*) exposes the nucleotide to the solvent to a greater degree than the GDP (*cyan*) and GTP (*blue*) closed interfaces, in which the top monomer covers the nucleotide. The buried surface between these FtsZ monomers increased from 1017 $Å^2$ for the open interface to 1107 (GDP) or 1168 $Å^2$ (GTP) for the closed interfaces, reflecting the existence of a stronger interaction in the closed state. The GDP-open interface may facilitate the previously observed nucleotide dissociation from FtsZ polymers (41) and GTP exchange. Relative differences in bending and twisting can also be observed in the pairwise alignments of representative dimers (Fig. S2), which indicate that the GDP-closed interface conformation is clearly bent and untwisted with respect to the GTP conformation. Finally, the stiffer PC filaments were curved, also occluding the nucleotide, indicating an allosteric effect of this FtsZ filament-stabilizing ligand on the intermonomer association interfaces.

We characterized the curvature of the three types of MD-simulated filaments by analyzing the intrinsic bending between monomers. We monitored the relative orientation of each pair of monomers throughout the final 100 ns of the trajectories, as described previously (24,42) (Fig. 2 *A*; see Fig. S3 for details). For this purpose, we analyzed eight contact interfaces per case, considering both MD runs and excluding the interfaces at the ends of the filaments to avoid border effects. The angle distributions of the intermonomer interfaces (Fig. 2 *B*) were relatively wide, highlighting the extent of the fluctuations. In all simulated cases, the distributions of the main bending angle θ_1 were centered at relatively small negative values that corresponded to closed interfaces covering the nucleotide. For the GDP filaments alone (Fig. 2 *B*, *green line*), an additional population emerged at $6.6 \pm 4.4°$, overlapping the closed-interface distribution ($-6.6 \pm 4.0°$) and indicating bending in the opposite opening direction.

Different interface configurations have been observed in MD simulations of the archaeal (MjFtsZ) dimer, in which single transitions from GDP-open to GDP-closed interfaces have been documented (24). Instead, we found that multiple intermediate conformations between the closed and open interfaces coexisted along the bacterial GDP filament during the simulation, which is indicative of a dynamic equilibrium. Fig. 2 *C* illustrates the dynamical changes of the bending angle θ_1 observed in an MD simulation of a single GDP filament at four monomer-monomer interfaces. During the first part of the simulation, we observed fluctuations between the GDP-open and GDP-closed interface configurations, but at the end, the filament consisted of heterogeneous interfaces that typically fluctuated around a given configuration (see Fig. 2 *C*). For example, the S-shaped GDP filament displayed in Fig. 1 *A* corresponds to alternating open and closed interfaces. In contrast, with GTP the interface between monomers remained closed during all simulation times (see Fig. S4). Note that to facilitate comparisons between different interfaces, we computed the bending angles using a fixed reference framework (*gray axes* in Fig. 2 *A*) aligned to the maximal bending amplitude of the GTP case. However, the direction of the maximal amplitude of the bending of other cases exhibits different orientations. The GDP-open bending points approximately toward the C-terminal end, whereas GDP-closed interface filaments point in the opposite direction. The maximal bending orientations of GTP and GDP-closed filaments deviate by 35°. For orientation purposes and comparison with the bending of the structural homolog tubulin, the FtsZ views in Fig. 2 *A* roughly correspond to tubulin viewed from the inside of the microtubule lumen and from the microtubule end. The bending direction of the hinge opening of the GDP interfaces would point toward the outside of a microtubule, which is comparable to the curvature in bent protofilaments peeling off at disassembling microtubule ends (43).

The bending of the PC filament ($-4.6° \pm 4.5°$) was similar to that of the GDP-closed interfaces. The largest amplitude for the closed conformation was found with the GTP interfaces ($-9.0° \pm 4.3°$), indicating a major closure of the GTP filaments. The relative differences in the second bending angle θ_2 were smaller. In this case, the values were $2.6° \pm 2.8°$ and $3.8° \pm 4.2°$ for the GDP- and PC-bound filaments, respectively, whereas the GTP filaments fluctuated around the initial straight position ($-0.3° \pm 3.7°$). Interestingly, the GTP filaments twisted, with Φ angles of $-10.2° \pm 4.8°$ between consecutive monomers, whereas

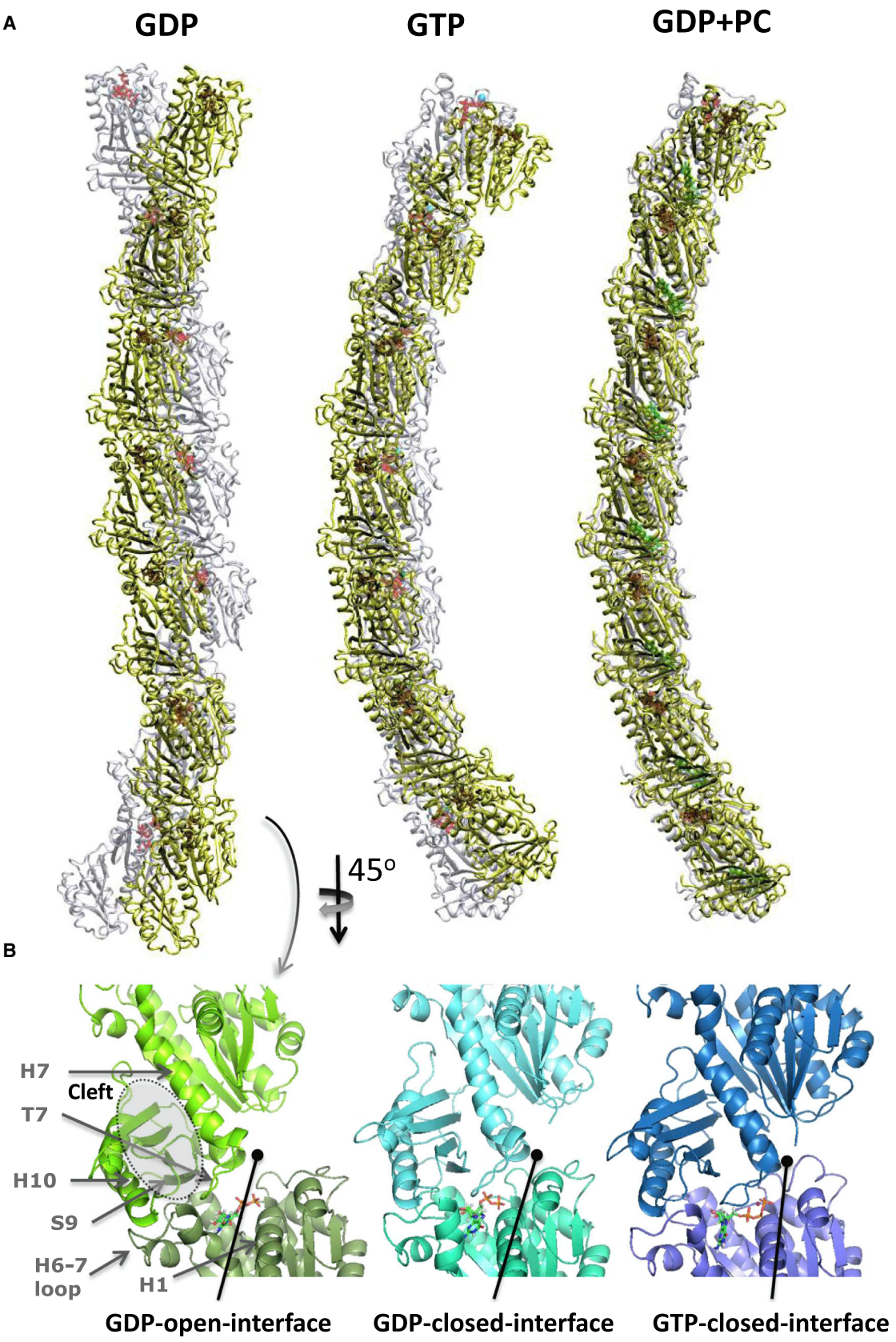

(legend on next page)

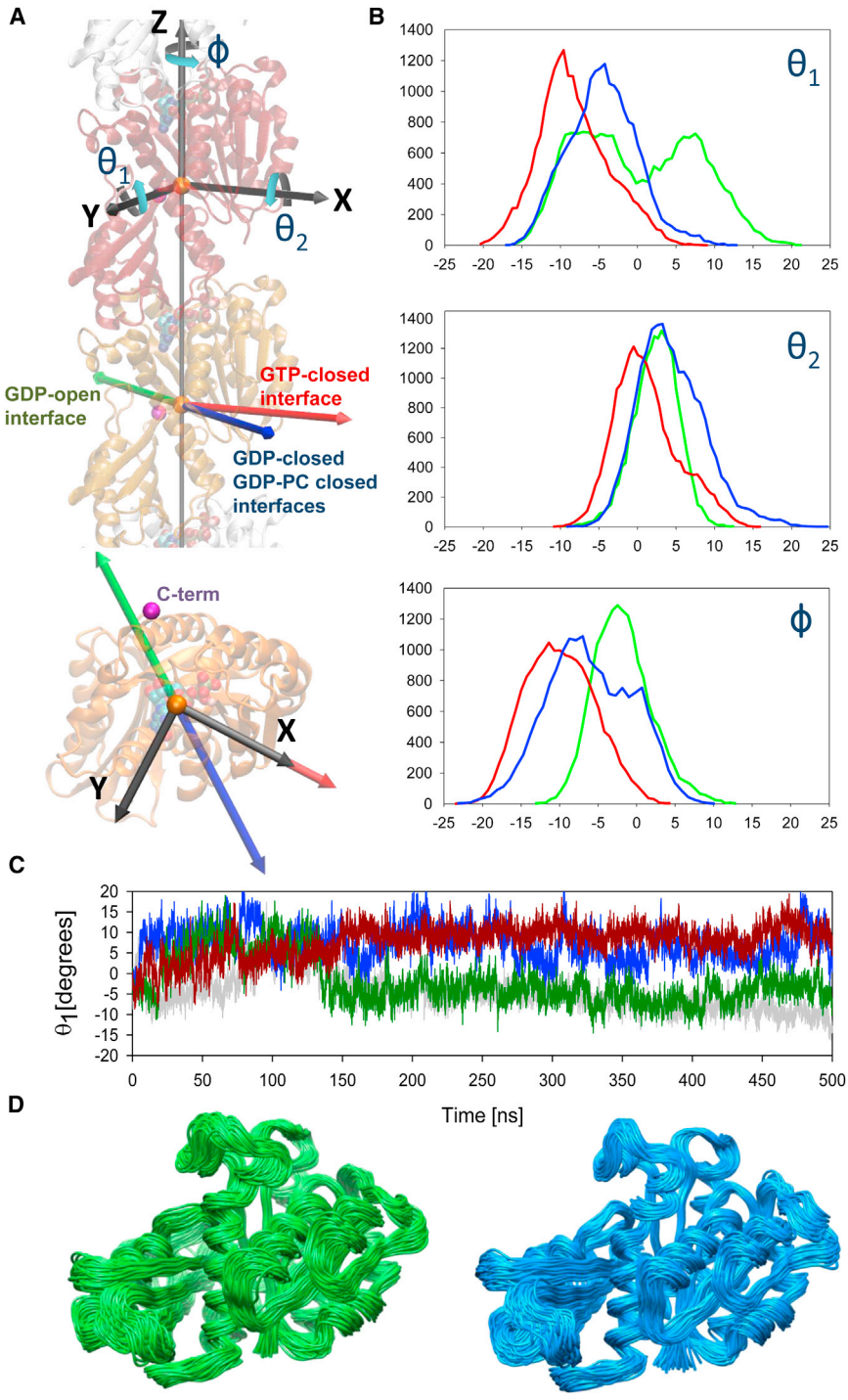

FIGURE 2 Characterization of interface conformations. (*A*) Coordinate frame used to calculate the relative rotations between consecutive monomers in the filaments. The rotation about the z axis, which is directed along the filament, describes the twist between consecutive monomers (Φ); the main bending angle θ_1 was chosen to lie in the maximal bending direction of the GTP filament; and the secondary bending angle θ_2 was defined around the x axis (see Fig. S3 for additional information). The maximal bending directions are represented with colored arrows for the GDP-open (*green*), GTP-closed (*red*), and GDP-closed (*blue*) intermonomer interface configurations and superimposed with the reference frame used to measure the bending angles (*gray*). The GDP-open maximal bending is directed approximately to the C-terminal domain, whereas GDP-closed interface filaments point in the opposite direction. The bending orientations of GTP and GDP-closed filaments deviate by 35°. Note that this view is roughly equivalent to tubulin viewed from the inside of a microtubule. The bottom image is a view along the z axis defined in the top image. (*B*) The plots represent the corresponding angle distributions for the GDP filament (*green*), GTP filament (*red*), and PC filament (*blue*) from the final 100 ns of the MD trajectories. (*C*) Time evolution of the main bending angle θ_1 for the four central interfaces of an illustrative GDP filament. Notice that the GDP filament converges to a heterogeneous filament formed by open (~6°) and closed (~−6°) interfaces. In contrast, the monomer association remains closed during all of the simulations for GTP and GDP-bound filaments (see Fig. S4) (*D*) Average conformations of representative monomers within GDP (*green*) and GTP (*blue*) filaments from the final 100 ns of the trajectory aligned by a maximum-likelihood superimposition criterion using THESEUS (1). To see this figure in color, go online.

the GDP filaments fluctuated around −2.2° ± 3.5°, and the PC filaments twisted by −6.2° ± 6.1° (Fig. 2 *B*). In our bacterial FtsZ filament MD simulation, the contacts with neighboring monomers at the interfaces naturally constrained the hinge-opening motion, reducing the bending amplitude toward more realistic moderately curved filament

FIGURE 1 (*A*) Snapshots of the FtsZ MD trajectories for a GDP filament, GTP filament, and GDP + PC filament viewed perpendicular to the average plane of bending of the GTP- and GDP-closed filaments (see text). In each case, the final filament structure after 300 ns (*colored ribbon*) is superimposed on a snapshot acquired during the previous 100 ns (*gray ribbon*). (*B*) Close-up views of illustrative dimer interfaces corresponding to GDP-open (*green*), GDP-closed (*cyan*), and GTP (*blue*) filaments. The orientation in this panel corresponds to the filament in panel *A* rotated by 45° around the filament axis. The secondary structure elements mentioned in the text are indicated. To see this figure in color, go online.

conformations (44). In contrast, one crystal structure of FtsZ from *Mycobacterium tuberculosis* FtsZ (MtFtsZ) (26) and the dimer simulations of MjFtsZ (24) and MtFtsZ (26) exhibited stronger bending.

Remarkably, the monomer structures within the GDP and GTP filaments appear very similar when compared with each other (Fig. 2 *D*). Therefore, the observed conformational changes resulted primarily from a rigid-body hinge movement between the monomers (see illustrative transitions using normal mode analysis (45) in Movie S2). In fact, the average root mean-square deviations (RMSDs) of the independently aligned monomers within the filaments are similar (Fig. S5). In both cases, the largest fluctuations were observed for the T3, T7, and H6-H7 loops, and for the C-terminal domain that fluctuated around the open-cleft conformation. Interestingly, the tip of H7 was consistently more bent for GTP than for GDP (Fig. 2 *D*). In the case of the PC filaments, the rigidity was reflected in lower monomer RMSDs (Fig. S5), although fluctuations of the H6-H7 loop and the C-terminal domain were still evident. Nevertheless, we found it intriguing that the stabilizing agent PC induced a filament conformation similar to that for GTP.

Rough estimates of macroscopic parameters were obtained based on the angle distributions. The average inward radial force produced per monomer in a filament is proportional to $\Delta\theta k_B T/(2l\sigma^2)$ (24), where $\Delta\theta$ is the mean bending-angle difference between two conformational states, σ is the variance of θ in the final conformation, l is the length of an FtsZ monomer (~4.0 nm), T is the temperature (298 K), and k_B is the Boltzmann constant. Based on the θ_1 angle distributions, hydrolysis from the GTP-closed to the GDP-open interface conformation yields 23 pN of inward bending force at each interface, and the smaller GTP to GDP-closed interface transition produces a force of 4 pN. The GDP-closed to GDP-open transition alone produces a significant force of 19 pN. Such interface transitions and a membrane-attachment element could provide the constriction force generated by FtsZ without the need for any other proteins (44,46). Previous MD simulations of MjFtsZ dimer (24) reported somewhat larger forces of 30 pN for the GTP to GDP-open transition, and 20 pN per monomer for the GTP to GDP-closed transition. However, all of these rough estimates are greater than the experimentally measured force of 5 pN generated by bending of a structurally related microtubule protofilament (47). In addition, homogeneous GDP-open and GDP-closed interface filaments are abstractions and, as was the case in our simulations, a variety of conformations coexist along the filament, allowing for different intermediate curved conformations and hence smaller effective constriction forces. The true picture must be even more complex, as FtsZ protofilaments contain a mixture of GDP- and GTP-bound subunits that can reach a ratio of 50:50 (48), and such subunits can undergo exchange within steady-state FtsZ filaments (49).

The mean radii of curvature for homogeneous filaments, estimated as l/θ_1, were 50 nm, 26 nm, and 35 nm for PC, GTP, and GDP-closed, respectively, whereas the GDP-open interface filament had the opposite curvature with a 35 nm radius. The curvature of the PC filament was compatible with the ~100-nm-diameter toroids observed by electron microscopy in carbon-adsorbed SaFtsZ polymers assembled with PC (see, for example, Fig. 8 *C* in Andreu et al. (8)). We note that these values are collectively one order of magnitude smaller than the ~1 μm diameter of a bacterial cell (50).

Our SaFtsZ filaments in silico are apparently quite flexible. The persistence length values computed according to the method described by Grafmüller and Voth (42) were 88 nm for GTP and 113 nm for GDP-PC filaments, which are much shorter than the value for microtubule protofilaments (42). The dynamic heterogeneity of the GDP filament curvature precluded the computation of reliable persistence length values. Comparison with current experimental measurements is difficult because the persistence length values are considerably larger than the heptamers simulated, and because of the large disparity in measurements found in the literature for GTP/GDP filaments of FtsZ from other species. For example, in a cryo-electron microscopy study of *Escherichia coli* FtsZ (EcFtsZ), Turner et al. (51) visualized relatively straight filaments with a persistence length of 1.4 μm. In contrast, we previously estimated protofilament persistence length values in the 100 nm range, also using cryo-electron microscopy of EcFtsZ but neglecting intrinsic filament curvature (17). Nevertheless, the disparity in persistence lengths can be visualized directly from the corresponding electron micrographs (see Fig. 1 in Turner et al. (51) versus Fig. 3 in Huecas et al. (17)). Moreover, these measurements were based only on the bending flexibility alone and ignored the torsional contribution; however, we observed a significant twist component in the GTP-filament simulations. The importance of filament twisting was recently highlighted (29) based on the high twisting polymorphism found in atomic force microscopy images of filaments attached to mica. On the other hand, negative-stain electron microscopy of FtsZ rings attached to the outside of 0.5-μm-diameter lipid tubules showed ribbons of laterally associated protofilaments (52).

Insights into the GTP/GDP regulation of interfacial interactions in FtsZ filaments

The differences in dynamic behavior and curvature between filaments are logically related to monomer interactions. In Fig. 3, the intermonomer contacts from the final 100 ns of each simulation are projected onto the corresponding top and bottom interfaces. At first glance, it appears that there were many common contacts, but clear differences existed depending on the conformational state. Both the GTP and GDP-closed interface configurations featured a closed

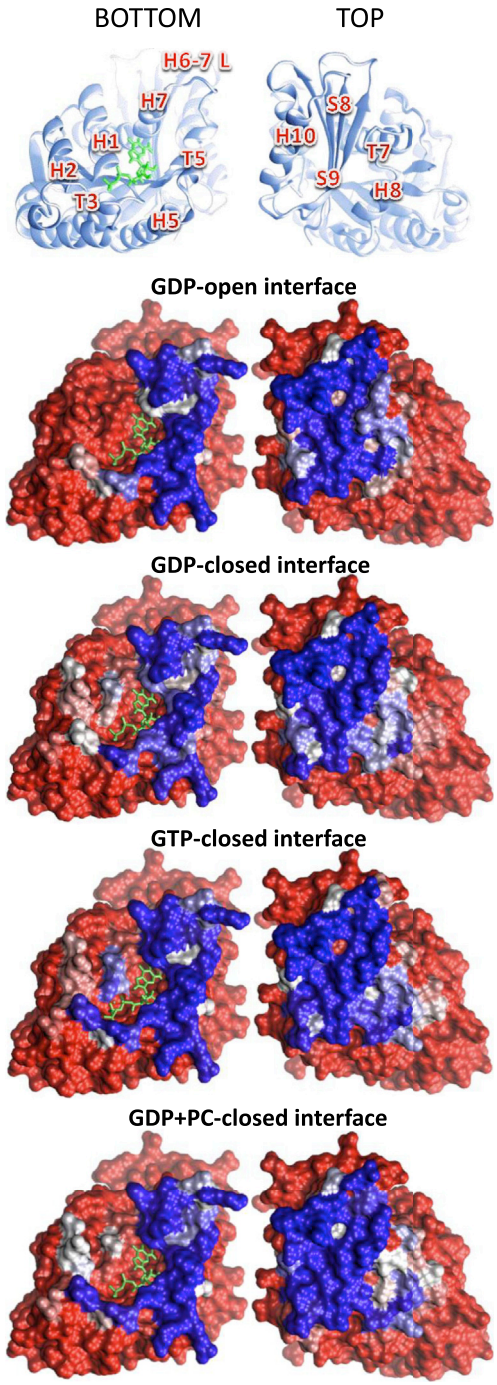

FIGURE 3 Interface contact surfaces. Intermonomer contacts were calculated between all pairs of residues from two consecutive filament FtsZ monomers. Two residues were considered to be in contact if they had at least one pair of atoms separated by <4 Å. The surface images correspond to the plus-end surface of the bottom monomer (*left*) and the minus-end surface of the top monomer (*right*). The presence of contacts during the simulation is projected on corresponding interface surfaces with a color ramp from red to white to blue. Blue regions correspond to contacts that were present throughout the entire simulation, white regions correspond to contacts that were present for 50% of the simulation, and red regions exhibited no contact at all. Contacts were only calculated for the four central monomer interfaces throughout the final 100 ns of the MD simulations. To see this figure in color, go online.

nucleotide-binding site and hence their contact patterns were quite similar. In the case of GTP, the binding site was fully enclosed, with stable contacts (*dark blue regions*) all around the nucleotide. In contrast, the GDP-closed interface exhibited less stable contacts (*lighter blue or white regions*) between the H1/H2/T3 regions of the bottom monomer and the H8/T7 region of the top monomer. Finally, the GDP-open interface configuration exhibited the smallest contact region, with fewer contacts between the H1 and H2 helices and the T7 loop, suggesting a weaker monomer-to-monomer association. Thus, we can identify two major monomer-monomer contact regions. The first region includes the common interactions of the N-terminal domain of the bottom monomer with the C-terminal domain (segments 260–300) of the top monomer. This region is shared by all filament interfaces and corresponds to the blue areas of Fig. 3 that are close to the center of each panel. This region includes the contacts of the top monomer's H10 helix and its flanking regions with the T5 and H6-H7 loops of the bottom monomer. A stable hydrogen bond links the H5 helix and the H10-S9 loop through the Arg-141 and Asp-289 residues, respectively. Other stable hydrogen bonds were established between Met-179 (loop H6-H7) and Leu-270 (H10), and between Lys-142 (H5) and Asp-213 (H8). Because we observed nearly the same contact pattern in each simulation (see the contact maps presented in Fig. S6), we believe that this first region constitutes the common anchor between monomers that supports the filament and acts as a hinge for opening the intermonomer interface.

The second characteristic contact region exhibits all of the differences among the filaments, and involves the contacts of the T7 loop and the H8 helix of the top monomer (residues 203–219) with the elements of the N-terminal domain of the bottom monomer. These contacts are represented by the blue and white areas in Fig. 3 that are missing in the GDP-open configuration. In the GTP and GDP-closed interface configurations, the T7 loop (Glu-206 and Asn-208) bound the bottom monomer's H1 and H2 helices (Asn-25, Arg-29, and Asp-46). Interestingly, whereas the H1 contact became stronger in the presence of the γ phosphate, all of the T7-loop interactions were missing in the GDP-open configuration. In a similar manner, H8 bound the T3 loop of the bottom monomer in the GTP filament, whereas the GDP-closed and GDP-open filaments exhibited progressively weaker contacts (Fig. S6). In the GTP filament, the first residue of H8, Asp-210, interacted with Gly-70, Ala-71, and Gly-72; however, this residue interacted only with the glycines in the GDP-closed interface and only with the alanine in the GDP-open interface. Additionally, the GDP-open interface lacked a hydrogen bond between Phe-138 (T5) and Gln-283 (H10) and an electrostatic interaction between Glu-206 (T7) and Lys-184 (H8), which were present in the closed filaments. A common feature of all GDP-bound filaments was the presence of a monovalent cation

or a water molecule at the T7 loop, which coordinated the main-chain carbonyl groups of Leu-200, Leu-209, Leu-210, and Val-203, and the side-chain carbonyl from Asn-208, Asp-46, and Glu-48. This coordination was present during the major part of the GDP simulations and it was hardly observed with GTP filaments. The majority of the contacts of the initial GDP crystal structure were present to a greater or lesser extent during the simulations, with the following exceptions: 1) contacts of top monomer loop T7 and helix H8 with bottom monomer H5 that were observed in the GTP and GDP filaments but lost in the PC-bound filament (Fig. S6); and 2), the key contacts made by the GTP γ phosphate and coordinated Mg^{2+} ion with the top monomer, since these elements are absent from the GDP crystal structure but were introduced in the MD simulations.

The key element that held the GTP-bound interface closed was the coordinated Mg^{2+} ion, which also stabilized GTP in a position suitable for hydrolysis. GTP was primarily bound by the bottom monomer, but in the filament the Mg^{2+} ion connected the γ and β phosphates to the T7 loop of the top subunit (Fig. S7). This additional intermonomer connection was supported by a stable interaction of the cation with Asn-208 from the T7 loop of the top monomer and by weaker interactions with the flanking Asp-210 (T7) and Asp-213 (H8). Two water molecules completed the Mg^{2+} coordination shell formed by γ phosphate, β phosphate, and Asn-208. Precisely one of these coordinated water molecules was located at the appropriate distance and orientation with respect to the γ phosphate for the hydrolysis reaction to occur. The polarization of this attacking water molecule could be produced by either one of the neighbor residues, Asp-210 or Asp-213, which were located at the correct hydrogen-bonding distance during our simulations. In addition, hydrogen bonds between Asn-208 and the α and β phosphates also stabilized the intermonomer contacts.

The FtsZ assembly switch mechanism and the interdomain cleft

It has been proposed that the ability of FtsZ to cooperatively assemble into single-stranded filaments is related to a change in monomer conformation that involves an opening movement of the C-terminal domain with respect to the core helix H7 (see Introduction) (17–21). An open-cleft monomer conformation has been identified in the structures of SaFtsZ monomers forming a single-stranded crystal filament in which the H7 helix downshifts and inserts the T7 loop into a wider pocket of the subunit below, creating an axial association between SaFtsZ monomers (9,10) that is tighter than in other FtsZs structures. Remarkably, in our GTP and GDP filament simulations, the open-cleft conformation was maintained, except for the minus-end monomer, which closed the cleft. To monitor this transition, we measured the distance between the centers of mass of the end of the H7 helix (residues 196–202) and the S9 β strand (residues 295–300) from the C-terminal domain. As shown in Fig. 4 *A*, during the simulation this distance fluctuated around the initial value of 13 Å in all monomers except the last one, for which the distance was reduced to 9 Å. The closure of the last monomer was observed in nearly all GTP and GDP simulations, suggesting the tendency of the FtsZ molecule to close the cleft when it is free from the restriction of a bottom subunit. To investigate this further, we performed two unbiased long MD simulations

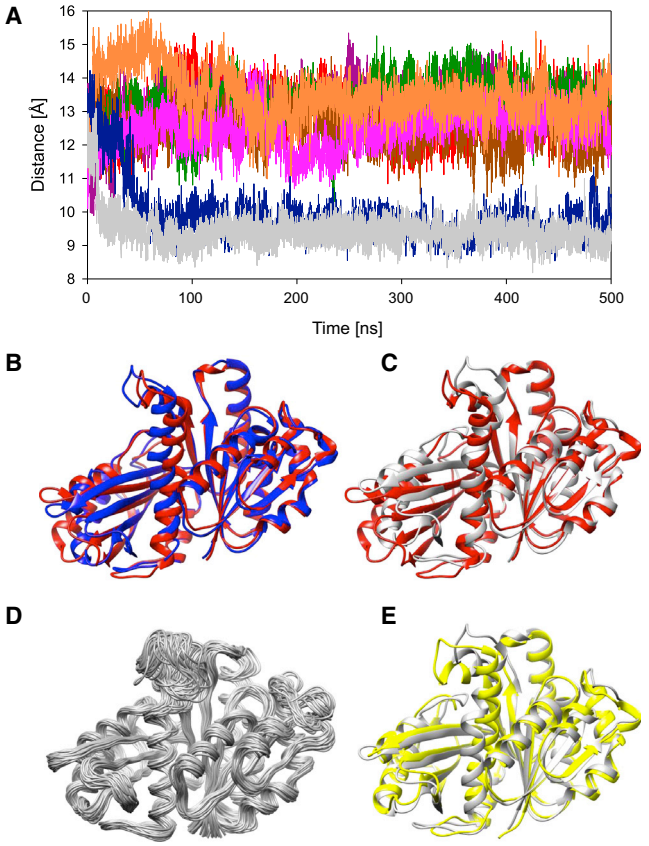

FIGURE 4 Relaxation of the FtsZ assembly switch. (*A*) Sample trajectories exhibiting closure of the interdomain cleft for the seven monomers in a GTP filament. The time evolution of the distance between the centers of mass of the end of the H7 helix (residues 196–202) and the S9 sheet (residues 295–300) during the MD simulation is shown. The distance fluctuated around the initial distance of 13 Å for all monomers in the filament except for the last monomer at the minus end, whose cleft closed by 4 Å, as indicated by the blue line. Similar results were observed for other GTP and GDP filaments, where the minus-end monomer quickly closed the cleft. The gray line corresponds to the more rapid closure detected in the simulations of an isolated monomer. For comparative proposes, we extended the simulation of the isolated monomer to 500 ns. (*B*) Superimposition of the initial filament open-switch structure (*red*) on the final MD closed-switch structure of the last monomer in the filament simulation (*blue*) and (*C*) on the isolated-monomer simulation (*gray*). (*D*) Maximum-likelihood superimposition of all monomer conformations during the final 100 ns in the isolated-monomer simulation. (E) The final closed-switch monomer structure (*gray*) superimposed on the crystallographic structure of *Bacillus subtilis* (*yellow*, PDB ID 2VXY). To see this figure in color, go online.

of an isolated open-cleft monomer bound to GTP or GDP. As before, the H7-S9 distance quickly decreased and underwent a spontaneous transition to the closed-cleft conformation (*gray line* in Fig. 4 *A*). The structural change of a SaFtsZ monomer during the transition from the actively associating open-cleft conformation to the low-affinity closed-cleft conformation is presented in Movie S3. The fact that the cleft of the minus-end and the isolated monomers remained closed during the major part of simulations is a good indicator of stability and hence sampling sufficiency (Fig. 4 *A*). The cleft closure can also be observed either by superimposing the initial open structure (*red*) on the final closed MD conformations of the minus-end (*blue*, Fig. 4 *B*) and free monomers (*white*, Fig. 4 *C*) or by comparing the ensemble average conformations of the closed isolated monomer (Fig. 4 *D*) with the open-filament conformations (Fig. 2 *D*). Collectively, these results reveal the natural tendency of monomeric SaFtsZ to adopt the closed-cleft conformation. Given the high structural homology among FtsZs, it is possible that other FtsZ family members may share this tendency. In fact, our closed-cleft SaFtsZ MD structure is closed similarly to other bacterial FtsZ monomer structures, as illustrated for the FtsZ of *Bacillus subtilis* (BsFtsZ) in Fig. 4 *E*. Despite their resemblance, however, and as expected from the variability observed in this region for the monomers simulations (Fig. 4 *D*), they do not superpose well in the tip of H7 and the loop H6-H7 regions. We observed a deformation of the top of the helix and the surrounding loops, rather than the C-terminal subdomain rotation that was previously observed with two SaFtsZ T7-loop deletion mutants with inhibited GTPase (53).

Thus far, the results of our extensive MD simulations have provided insight into bacterial FtsZ filament dynamics and the nucleotide regulation of association interfaces between FtsZ monomers. These findings support the physiological relevance of the SaFtsZ filament crystal structure and confirm the existence of the structural assembly switch by employing the same FtsZ protein that was previously inferred only through comparisons of different structures (9,11).

Mechanism of FtsZ filament stabilization by antibiotic PC190723

The curvature of the GDP + PC filaments in our MD simulations resembled that of the GTP filaments; however, the stabilization mechanism of the stiffer PC filament was distinct. Whereas the GTP γ phosphate and Mg^{2+} directly linked adjacent FtsZ monomers in the GTP filament, PC allosterically induced the closure of the intermonomer interface by blocking the assembly switch in the active conformation. The presence of PC stabilized the contacts of the top monomer's T7 loop with the bottom monomer's H2 and H1 helices and impeded those observed in other filaments with bottom H5 helix (Fig. S6). The stabilization of the T7 loop promoted closure of the intermonomer interface, causing the filament to curve in a manner similar to what was observed in the GTP case, but in a slightly different direction (Figs. 1–3). The PC interfaces curved in same direction as the GDP-closed configuration (Fig. 2 *A*), whereas the GTP filament bent 35° apart, enclosing the nucleotide more tightly. In contrast to the free GDP filaments, the PC-bound filaments were twisted as in the GTP case. This behavior increased the interfacial packing in the PC filament, reducing the intrinsic flexibility of the monomer (Fig. S5). Our simulation results are fully consistent with experimental observations of the stabilizing effect of this compound in the close homolog BsFtsZ (8). Because this ligand binds to the interdomain cleft, it also held open the minus-end subunit of the filament, in contrast to the behavior observed in the GTP and GDP filaments without PC.

Filament-stabilizing effect of Ca^{2+} ions

We initially omitted the Ca^{2+} ion found in the crystallographic filament structures of SaFtsZ from the MD simulations because no other FtsZ structures contain this cation and because the Ca^{2+} concentrations that affect SaFtsZ polymerization and GTPase are rather high (1–10 mM) (11). Moreover, a nearly identical calcium-free SaFtsZ filament structure was recently documented (54). Nevertheless, we examined the effects of the Ca^{2+} ion in the GDP and PC filaments by performing equivalent long MD simulations. In contrast to the calcium-free situation, the interfaces of the Ca^{2+}-GDP filament were closed, resulting in a more stable curved filament. As in the crystal structure, the Ca^{2+} was coordinated with two water molecules inside the T7 loop, supporting an apparent increase in the intermonomer contact near H2 (see Fig. S8). Because the PC filament was already quite rigid, we were unable to detect any further differences caused by the presence of Ca^{2+} in terms of relative stability. Interestingly, isolated SaFtsZ monomers spontaneously lost their bound Ca^{2+} during the MD simulations, as did the last monomer at the minus-end of the filament. These results suggest that the Ca^{2+} ion plays a secondary role in stabilizing the T7 loop in FtsZ filaments.

DISCUSSION

Nucleotide-regulated FtsZ filament interfacial dynamics

Our MD simulations of representative bacterial FtsZ filament structures demonstrated that nucleotide-dependent intermonomer contacts play a key role in controlling the intrinsic curvature of the filaments and, by extension, their stability. In agreement with the experimentally observed polymorphism of FtsZ protofilaments, we found different filament curvatures supported by a nucleotide-regulated hinge motion between interfacial subunits. Revealing a

high intrinsic variability, the GDP-bound filaments fluctuated among various curved conformations, forming a heterogeneous distribution of open and closed interfaces. By contrast, locking the intermonomer nucleotide site, the GTP-bound filaments converged to less flexible polymers that curved in a preferred orientation. The conformational changes of this highly dynamic equilibrium associated with GTP hydrolysis may provide a structural basis for the initial Z-ring constriction. The coordinated Mg^{2+} contributed significantly to monomer binding in the GTP filament by tightly connecting the T7 loop of the top subunit to the nucleotide firmly attached to the bottom subunit. This interaction closed the binding pocket, thereby stabilizing the GTP in a conformation suitable for hydrolysis. Another important element of the hinge was the intrinsic flexibility of the H6-H7 loop and the tip of the H7 helix of the bottom subunit, which facilitated the complementarity between adjacent subunits and eventually helped to transmit a conformational change through H7 from one FtsZ monomer to another along the filament. Although we observed flexibility in the T3 loop, the relative differences for this loop in the MD simulations of the GTP and GDP filaments provide no evidence for a hydrolysis-dependent conformational switch supporting the bending between subunits at this loop, as postulated by others (26). Although the GTP γ phosphate can actually pull away from the T3 loop in isolated FtsZ monomers (55), we think that the γ phosphate and the coordinated Mg^{2+} ion play the major role in FtsZ filament stability.

The intrinsically curved FtsZ filaments may generate a bending force on a much less curved membrane without the need for GTP hydrolysis (56). Intermediate curvatures have also been observed in atomic force microscopy images of FtsZ protofilaments adsorbed on mica (57–59) and in FtsZ polymers attached to engineered membranes (3). In addition, the torsion of spontaneously twisted FtsZ filaments caused by side attachment to mica or membrane surfaces should generate filament curvature and force (29). Our MD simulations indicate clear differences in the average curvature and twist between GTP- and GDP-FtsZ filaments, which suggest that the GTP/GDP balance in the FtsZ filaments modulates their attachment to the membrane through FtsA and ZipA, as well as any resulting mechanical function in bacterial cells. The straighter or more curved filament conformations observed by microscopy could also be influenced by additional interactions experienced by the C-terminal FtsZ tails. It is known that the flexible C-terminal linker and the constant and variable zones of the C-terminus, which are absent in the crystal structures and MD simulations, participate in FtsZ polymerization, FtsZ filament tethering to the membrane, and Z-ring formation (60,61).

Mutations at interfacial residues affect the stability of filaments, which further demonstrates the importance of the intermonomer contact regions (20,26,62,63). Many of these interfacial mutations affect cell division, but FtsZ can still polymerize into filaments, indicating that the Z-ring constriction can be disrupted by a defect in the filament dynamics. Interestingly, an FtsZ mutation at a key Mg^{2+}-binding residue, Asp208Ala, resulted in a lack of polymerization even in the presence of calcium ions (see Fig. 8 in Matsui et al. (11)). To explain this result, Matsui et al. (11) proposed that the coordination of Ca^{2+} with Asp-208 stabilizes the GTP polymer, thereby slowing the hydrolysis to GDP. By contrast, our simulations demonstrated the importance of this residue in anchoring the upper monomer through the coordinated Mg^{2+}. The same authors recently presented mutagenesis results concerning the T7 loop in SaFtsZ (54). They replaced the T7-loop sequence (VSGEV) with that of BsFsZ (TPGLI) without affecting the GTPase activity. This result provides further evidence of common interface contacts between different FtsZs and the representativeness of the SaFtsZ filament structure. Two T7-loop deletion mutants with inhibited GTPase showed domain movements; however, they still crystallized as straight protofilaments (38). It would be worthwhile to determine, using the appropriate mutants, which crystal-packing contacts make SaFtsZ form straight protofilaments in different space groups, in contrast to other FtsZs. Nevertheless, SaFtsZ protofilaments did curve both during our MD simulations and when adsorbed to carbon onto electron microscope grids.

Association-induced activation switch of FtsZ monomers

The cooperative assembly of FtsZ is related to a conformational change that involves the opening and closing of the cleft between the C-terminal domain and the H7 helix (20,21). In our simulations, we observed a closure of the minus-end monomer in the filament and the natural tendency of the isolated monomer to adopt a relaxed closed-cleft conformation. These results support the presence of a conformational equilibrium between the low-affinity closed-cleft and active filament-forming open-cleft conformations that was previously inferred from comparisons among structures of different FtsZs (9,11), but had not yet been observed in the same FtsZ protein. Interestingly, in Matsui et al. (54), the truncated GDP-bound chimeras $\Delta T7_{GAG}$ and $\Delta T7_{GAN}$ yielded closed-cleft structures similar to those observed for BsFtsZ, whereas GTP-$\Delta T7_{GAN}$ maintained the wild-type open conformation. The structures of such GDP-bound chimeras are similar to the closed-cleft conformation observed in the monomeric state. Thus, we suggest that the nucleotide-dependent change observed by these authors reflects the transition between actively associating and inactive monomers rather than a real change produced in the filament. Although the chimeras exhibited no GTPase activity (likely attributable to defective polymerization), these results also suggest that the contacts of the T7 loop, particularly those related to γ phosphate or Mg^{2+}, play a pivotal role in controlling the activation switch. In contrast to typical GTPase switches, in which the nucleotide

binding induces an activating conformational change in the unassociated protein (64), the unassembled states of FtsZ and its eukaryotic homolog, tubulin (5,23), are predominantly inactive and switch to the active forms by assembly contacts with the aid of GTP binding, which lowers the corresponding free-energy barrier (53). Note that for accuracy, we have intentionally avoided using the terms "curved" and "straight" because we observed dynamically curved FtsZ filaments in all of our simulations. In fact, regardless of the sampling limitations, our results clearly indicate the intrinsic instability of straight FtsZ filaments.

Mimicking a nondisassembling GTP filament with PC190723

The binding of PC stabilizes the FtsZ filament in a bent conformation similar to that observed for the GTP filaments. PC permanently holds the interdomain cleft open, in opposition to the natural tendency of the monomer to adopt the closed-cleft conformation. As a result of internal movements, this cell-division inhibitor allosterically stabilizes a closed intermonomer interface with additional links between the top T7 loop and H8 helix and the H2 helix of the bottom monomer. Because the PC binding site is occluded in the FtsZ monomer, it is likely that this compound binds only to the open-cleft conformation, displacing the equilibrium toward the high-affinity conformation required for FtsZ polymer elongation. This switching to the conformation for polymerization explains the cooperative critical concentration behavior of PC-induced FtsZ polymerization (17). Regardless, there is no exact equivalence for the PC binding site in tubulin. The general stabilization mechanism is partially related to that of microtubule-stabilizing agents, which bind lateral contact elements that hold protofilaments together and thus suppress the monomer disassembly switch.

FtsZ assembly-disassembly cycle

The nucleotide-dependent filament dynamics and the assembly switch can be integrated into the FtsZ assembly-disassembly cycle schematically illustrated in Fig. 5. In an initial, moderately curved GTP filament, the interdomain clefts are open and the intermonomer interfaces are closed, poised for nucleotide hydrolysis. GTP hydrolysis then cuts the links formed by the γ phosphate and the Mg^{2+} between adjacent monomers, yielding a filament that is more flexible and prone to depolymerization. The intermonomer interfaces in an all-GDP model filament fluctuate between the open and closed states, whereas the monomer clefts remain open. The transition from the GTP-closed to the GDP-closed and GDP-open interface conformations could contribute to the constriction of the FtsZ rings in bacterial cells or reconstituted systems. The GDP filament

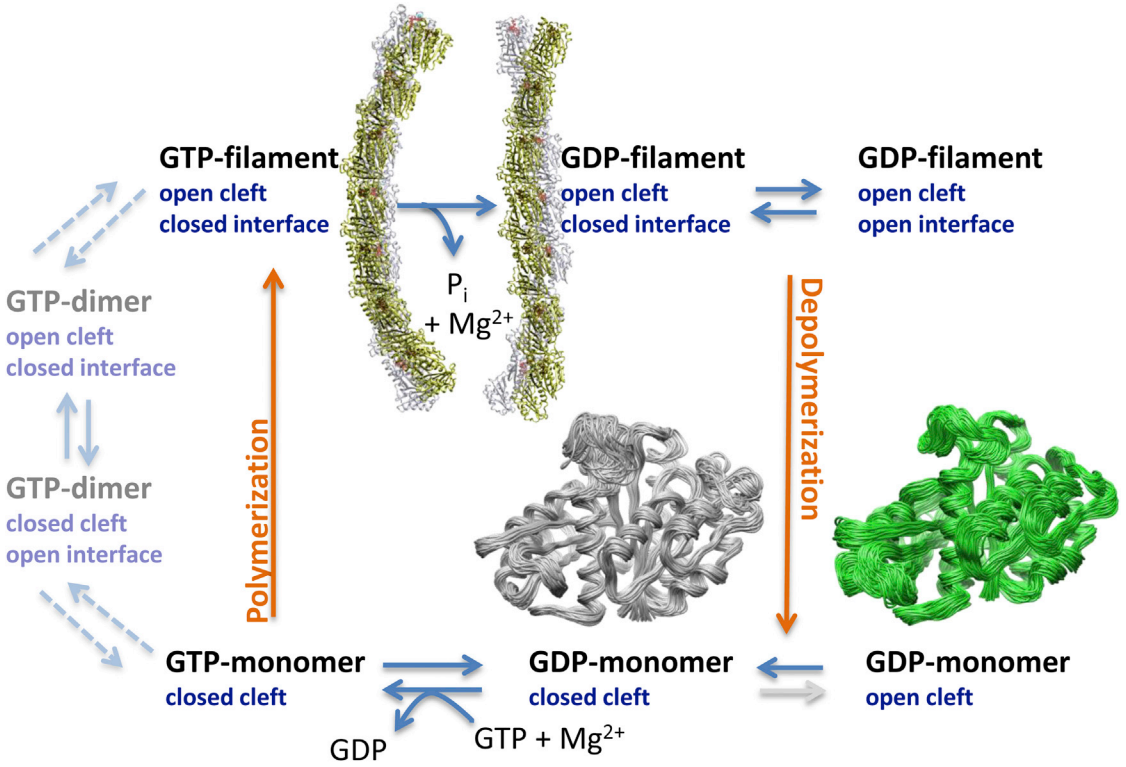

FIGURE 5 Scheme of the FtsZ assembly-disassembly cycle mechanism constructed by integrating the nucleotide-dependent filament dynamics and the assembly switch. See the main text for details. To see this figure in color, go online.

depolymerizes into GDP monomers whose interdomain clefts rapidly close (alternatively, some subunits might back-exchange GTP into the filament). The bound GDP spontaneously exchanges with GTP (which is present in excess), producing closed-cleft GTP monomers that are ready for polymerization. The assembly of the GTP-FtsZ monomers into a new filament is associated with the opening of their clefts through a mechanism that we cannot currently address using all-atom MD simulations. However, based on the properties of the system, one possibility is that GTP monomers with closed clefts initially associate as weak open-interface dimers or trimers. These inactive oligomers then isomerize into a tighter closed-interface active oligomer with an open plus-end monomer cleft, which constitutes a linear polymerization nucleus (17) that further elongates to form the filament (see the scheme of Fig. 5). How the observed conformational changes can be integrated to explain the cooperative assembly behavior remains an intriguing issue. To this end, both the top and bottom interfaces of a monomer must simultaneously switch to the high-affinity form (19). Our simulations clearly identified the cleft closure as the necessary conformational change at the bottom interface. However, we have only characterized the high flexibility of the tip of the H7 helix and the H6-H7 loops, which we speculate would sustain the conformational change at the top interface. We note that in addition to cooperative assembly, individual FtsZ filaments are also capable of treadmilling and fragmenting (4), as well as associating among themselves and with divisomal partners. The latter processes, in combination with assembly and disassembly, most likely constitute the constriction mechanisms of the Z-ring during cell division. Our findings shed new (to our knowledge) light on the structural basis of the FtsZ assembly process itself, in which two linked hinge motions, one located at the intermonomer interface and one at the cleft between monomer domains, modulate filament stability and dynamics in a remarkably simple manner.

SUPPORTING MATERIAL

Eight figures, and three movies are available at http://www.biophysj.org/biophysj/supplemental/S0006-3495(14)01007-8.

The authors gratefully acknowledge the computer resources, technical expertise, and assistance provided by the Red Española de Supercomputación. We thank Eva G. Noya for her assistance in simulation analysis, and M.A. Oliva and J.F. Díaz for their critical comments and suggestions. This study was supported by grants BFU2013-44306P (P.C.), BFU 2011-23416 (J.M.A.), and CM S2010/BMD-2353 (J.M.A. and P.C.), and by a CSIC-JAE fellowship supported by European Social Funds (E.R-A.).

REFERENCES

1. Theobald, D. L., and D. S. Wuttke. 2008. Accurate structural correlations from maximum likelihood superpositions. *PLOS Comput. Biol.* 4:e43.
2. Osawa, M., D. E. Anderson, and H. P. Erickson. 2008. Reconstitution of contractile FtsZ rings in liposomes. *Science.* 320:792–794.
3. Arumugam, S., G. Chwastek, …, P. Schwille. 2012. Surface topology engineering of membranes for the mechanical investigation of the tubulin homologue FtsZ. *Angew. Chem. Int. Ed. Engl.* 51:11858–11862.
4. Loose, M., and T. J. Mitchison. 2014. The bacterial cell division proteins FtsA and FtsZ self-organize into dynamic cytoskeletal patterns. *Nat. Cell Biol.* 16:38–46.
5. Nogales, E., K. H. Downing, …, J. Löwe. 1998. Tubulin and FtsZ form a distinct family of GTPases. *Nat. Struct. Biol.* 5:451–458.
6. Schaffner-Barbero, C., M. Martín-Fontecha, …, J. M. Andreu. 2012. Targeting the assembly of bacterial cell division protein FtsZ with small molecules. *ACS Chem. Biol.* 7:269–277.
7. Haydon, D. J., N. R. Stokes, …, L. G. Czaplewski. 2008. An inhibitor of FtsZ with potent and selective anti-staphylococcal activity. *Science.* 321:1673–1675.
8. Andreu, J. M., C. Schaffner-Barbero, …, A. J. Martín-Galiano. 2010. The antibacterial cell division inhibitor PC190723 is an FtsZ polymer-stabilizing agent that induces filament assembly and condensation. *J. Biol. Chem.* 285:14239–14246.
9. Elsen, N. L., J. Lu, …, K. J. Lumb. 2012. Mechanism of action of the cell-division inhibitor PC190723: modulation of FtsZ assembly cooperativity. *J. Am. Chem. Soc.* 134:12342–12345.
10. Tan, C. M., A. G. Therien, …, T. Roemer. 2012. Restoring methicillin-resistant Staphylococcus aureus susceptibility to β-lactam antibiotics. *Sci. Transl. Med.* 4:126ra135.
11. Matsui, T., J. Yamane, …, I. Tanaka. 2012. Structural reorganization of the bacterial cell-division protein FtsZ from Staphylococcus aureus. *Acta Crystallogr. Sect. D Biol Crystallogr.* 68:1175–1188.
12. Läppchen, T., V. A. Pinas, …, T. den Blaauwen. 2008. Probing FtsZ and tubulin with C8-substituted GTP analogs reveals differences in their nucleotide binding sites. *Chem. Biol.* 15:189–199.
13. Marcelo, F., S. Huecas, …, J. M. Andreu. 2013. Interactions of bacterial cell division protein FtsZ with C8-substituted guanine nucleotide inhibitors. A combined NMR, biochemical and molecular modeling perspective. *J. Am. Chem. Soc.* 135:16418–16428.
14. Chan, F. Y., N. Sun, …, K. Y. Wong. 2013. Identification of a new class of FtsZ inhibitors by structure-based design and in vitro screening. *J. Chem. Inf. Model.* 53:2131–2140.
15. Ruiz-Avila, L. B., S. Huecas, …, J. M. Andreu. 2013. Synthetic inhibitors of bacterial cell division targeting the GTP-binding site of FtsZ. *ACS Chem. Biol.* 8:2072–2083.
16. Keffer, J. L., S. Huecas, …, C. A. Bewley. 2013. Chrysophaentins are competitive inhibitors of FtsZ and inhibit Z-ring formation in live bacteria. *Bioorg. Med. Chem.* 21:5673–5678.
17. Huecas, S., O. Llorca, …, J. M. Andreu. 2008. Energetics and geometry of FtsZ polymers: nucleated self-assembly of single protofilaments. *Biophys. J.* 94:1796–1806.
18. Dajkovic, A., A. Mukherjee, and J. Lutkenhaus. 2008. Investigation of regulation of FtsZ assembly by SulA and development of a model for FtsZ polymerization. *J. Bacteriol.* 190:2513–2526.
19. Miraldi, E. R., P. J. Thomas, and L. Romberg. 2008. Allosteric models for cooperative polymerization of linear polymers. *Biophys. J.* 95:2470–2486.
20. Martín-Galiano, A. J., R. M. Buey, …, J. M. Andreu. 2010. Mapping flexibility and the assembly switch of cell division protein FtsZ by computational and mutational approaches. *J. Biol. Chem.* 285:22554–22565.
21. Chen, Y., and H. P. Erickson. 2011. Conformational changes of FtsZ reported by tryptophan mutants. *Biochemistry.* 50:4675–4684.
22. Oliva, M. A., D. Trambaiolo, and J. Löwe. 2007. Structural insights into the conformational variability of FtsZ. *J. Mol. Biol.* 373:1229–1242.
23. Oliva, M. A., S. C. Cordell, and J. Löwe. 2004. Structural insights into FtsZ protofilament formation. *Nat. Struct. Mol. Biol.* 11:1243–1250.

24. Hsin, J., A. Gopinathan, and K. C. Huang. 2012. Nucleotide-dependent conformations of FtsZ dimers and force generation observed through molecular dynamics simulations. *Proc. Natl. Acad. Sci. USA.* 109: 9432–9437.
25. Jamous, C., N. Basdevant, and T. Ha-Duong. 2014. Influence of GTP/GDP and magnesium ion on the solvated structure of the protein FtsZ: a molecular dynamics study. *J. Biomol. Struct. Dyn.* 32:916–927.
26. Li, Y., J. Hsin, …, S. Ye. 2013. FtsZ protofilaments use a hinge-opening mechanism for constrictive force generation. *Science.* 341:392–395.
27. Mendieta, J., A. I. Rico, …, P. Gómez-Puertas. 2009. Structural and functional model for ionic (K(+)/Na(+)) and pH dependence of GTPase activity and polymerization of FtsZ, the prokaryotic ortholog of tubulin. *J. Mol. Biol.* 390:17–25.
28. Natarajan, K., and S. Senapati. 2013. Probing the conformational flexibility of monomeric FtsZ in GTP-bound, GDP-bound, and nucleotide-free states. *Biochemistry.* 52:3543–3551.
29. González de Prado Salas, P., I. Hörger, …, P. Tarazona. 2014. Torsion and curvature of FtsZ filaments. *Soft Matter.* 10:1977–1986.
30. Van Der Spoel, D., E. Lindahl, …, H. J. Berendsen. 2005. GROMACS: fast, flexible, and free. *J. Comput. Chem.* 26:1701–1718.
31. Hess, B., C. Kutzner, …, E. Lindahl. 2008. GROMACS 4: algorithms for highly efficient, load-balanced, and scalable molecular simulation. *J. Chem. Theory Comput.* 4:435–447.
32. Hornak, V., R. Abel, …, C. Simmerling. 2006. Comparison of multiple Amber force fields and development of improved protein backbone parameters. *Proteins.* 65:712–725.
33. Salomon-Ferrer, R., D. A. Case, and R. C. Walker. 2013. An overview of the Amber biomolecular simulation package. *Wiley Interdiscip. Rev. Comput. Mol. Sci.* 3:198–210.
34. Wang, J., R. M. Wolf, …, D. A. Case. 2004. Development and testing of a general amber force field. *J. Comput. Chem.* 25:1157–1174.
35. Jorgensen, W. L., J. Chandrasekhar, …, M. L. Klein. 1983. Comparison of simple potential functions for simulating liquid water. *J. Chem. Phys.* 79:926–935.
36. Berendsen, H. J. C., J. P. M. Postma, …, J. R. Haak. 1984. Molecular dynamics with coupling to an external bath. *J. Chem. Phys.* 81:3684–3690.
37. Bussi, G., D. Donadio, and M. Parrinello. 2007. Canonical sampling through velocity rescaling. *J. Chem. Phys.* 126:014101.
38. Hess, B., H. Bekker, …, J. G. E. M. Fraaije. 1997. LINCS: a linear constraint solver for molecular simulations. *J. Comput. Chem.* 18:1463–1472.
39. Miyamoto, S., and P. A. Kollman. 1992. Settle: an analytical version of the SHAKE and RATTLE algorithm for rigid water models. *J. Comput. Chem.* 13:952–962.
40. Darden, T., D. York, and L. Pedersen. 1993. Particle mesh Ewald. An N-log(N) method for Ewald sums in large systems. *J. Chem. Phys.* 98:10089–10092.
41. Huecas, S., C. Schaffner-Barbero, …, J. M. Andreu. 2007. The interactions of cell division protein FtsZ with guanine nucleotides. *J. Biol. Chem.* 282:37515–37528.
42. Grafmüller, A., and G. A. Voth. 2011. Intrinsic bending of microtubule protofilaments. *Structure.* 19:409–417.
43. Alushin, G. M., G. C. Lander, …, E. Nogales. 2014. High-resolution microtubule structures reveal the structural transitions in $\alpha\beta$-tubulin upon GTP hydrolysis. *Cell.* 157:1117–1129.
44. Erickson, H. P. 2009. Modeling the physics of FtsZ assembly and force generation. *Proc. Natl. Acad. Sci. USA.* 106:9238–9243.
45. Lopéz-Blanco, J. R., J. I. Garzón, and P. Chacón. 2011. iMod: multipurpose normal mode analysis in internal coordinates. *Bioinformatics.* 27:2843–2850.
46. Erickson, H. P., D. E. Anderson, and M. Osawa. 2010. FtsZ in bacterial cytokinesis: cytoskeleton and force generator all in one. *Microbiol. Mol. Biol. Rev.* 74:504–528.
47. Grishchuk, E. L., M. I. Molodtsov, …, J. R. McIntosh. 2005. Force production by disassembling microtubules. *Nature.* 438:384–388.
48. Osawa, M., and H. P. Erickson. 2011. Inside-out Z rings—constriction with and without GTP hydrolysis. *Mol. Microbiol.* 81:571–579.
49. Chen, Y., and H. P. Erickson. 2009. FtsZ filament dynamics at steady state: subunit exchange with and without nucleotide hydrolysis. *Biochemistry.* 48:6664–6673.
50. Moran, U., R. Phillips, and R. Milo. 2010. SnapShot: key numbers in biology. *Cell.* 141:1262–1262.e1.
51. Turner, D. J., I. Portman, …, M. S. Turner. 2012. The mechanics of FtsZ fibers. *Biophys. J.* 102:731–738.
52. Milam, S. L., M. Osawa, and H. P. Erickson. 2012. Negative-stain electron microscopy of inside-out FtsZ rings reconstituted on artificial membrane tubules show ribbons of protofilaments. *Biophys. J.* 103: 59–68.
53. Buey, R. M., J. F. Díaz, and J. M. Andreu. 2006. The nucleotide switch of tubulin and microtubule assembly: a polymerization-driven structural change. *Biochemistry.* 45:5933–5938.
54. Matsui, T., X. Han, …, I. Tanaka. 2014. Structural change in FtsZ Induced by intermolecular interactions between bound GTP and the T7 loop. *J. Biol. Chem.* 289:3501–3509.
55. Díaz, J. F., A. Kralicek, …, J. M. Andreu. 2001. Activation of cell division protein FtsZ. Control of switch loop T3 conformation by the nucleotide gamma-phosphate. *J. Biol. Chem.* 276:17307–17315.
56. Osawa, M., and H. P. Erickson. 2013. Liposome division by a simple bacterial division machinery. *Proc. Natl. Acad. Sci. USA.* 110:11000–11004.
57. Hamon, L., D. Panda, …, D. Pastré. 2009. Mica surface promotes the assembly of cytoskeletal proteins. *Langmuir.* 25:3331–3335.
58. Lu, C., M. Reedy, and H. P. Erickson. 2000. Straight and curved conformations of FtsZ are regulated by GTP hydrolysis. *J. Bacteriol.* 182:164–170.
59. Mateos-Gil, P., A. Paez, …, M. Vélez. 2012. Depolymerization dynamics of individual filaments of bacterial cytoskeletal protein FtsZ. *Proc. Natl. Acad. Sci. USA.* 109:8133–8138.
60. Buske, P. J., and P. A. Levin. 2013. A flexible C-terminal linker is required for proper FtsZ assembly in vitro and cytokinetic ring formation in vivo. *Mol. Microbiol.* 89:249–263.
61. Gardner, K. A., D. A. Moore, and H. P. Erickson. 2013. The C-terminal linker of Escherichia coli FtsZ functions as an intrinsically disordered peptide. *Mol. Microbiol.* 89:264–275.
62. Stricker, J., and H. P. Erickson. 2003. In vivo characterization of Escherichia coli ftsZ mutants: effects on Z-ring structure and function. *J. Bacteriol.* 185:4796–4805.
63. Redick, S. D., J. Stricker, …, H. P. Erickson. 2005. Mutants of FtsZ targeting the protofilament interface: effects on cell division and GTPase activity. *J. Bacteriol.* 187:2727–2736.
64. Cherfils, J., and M. Zeghouf. 2011. Chronicles of the GTPase switch. *Nat. Chem. Biol.* 7:493–495.

Supporting Information

Understanding nucleotide-regulated FtsZ filament dynamics and the monomer assembly switch with large-scale atomistic simulations

Erney Ramírez-Aportela[1,2], Jose Ramón López-Blanco[1], José Manuel Andreu[2], Pablo Chacón[1]

[1]Department of Biological Physical Chemistry, Instituto de Química-Física Rocasolano, CSIC, Serrano 119. 28006 Madrid.

[2]Department of Chemical and Physical Biology, Centro de Investigaciones Biológicas, CSIC, Ramiro de Maeztu, 9. 28040 Madrid.

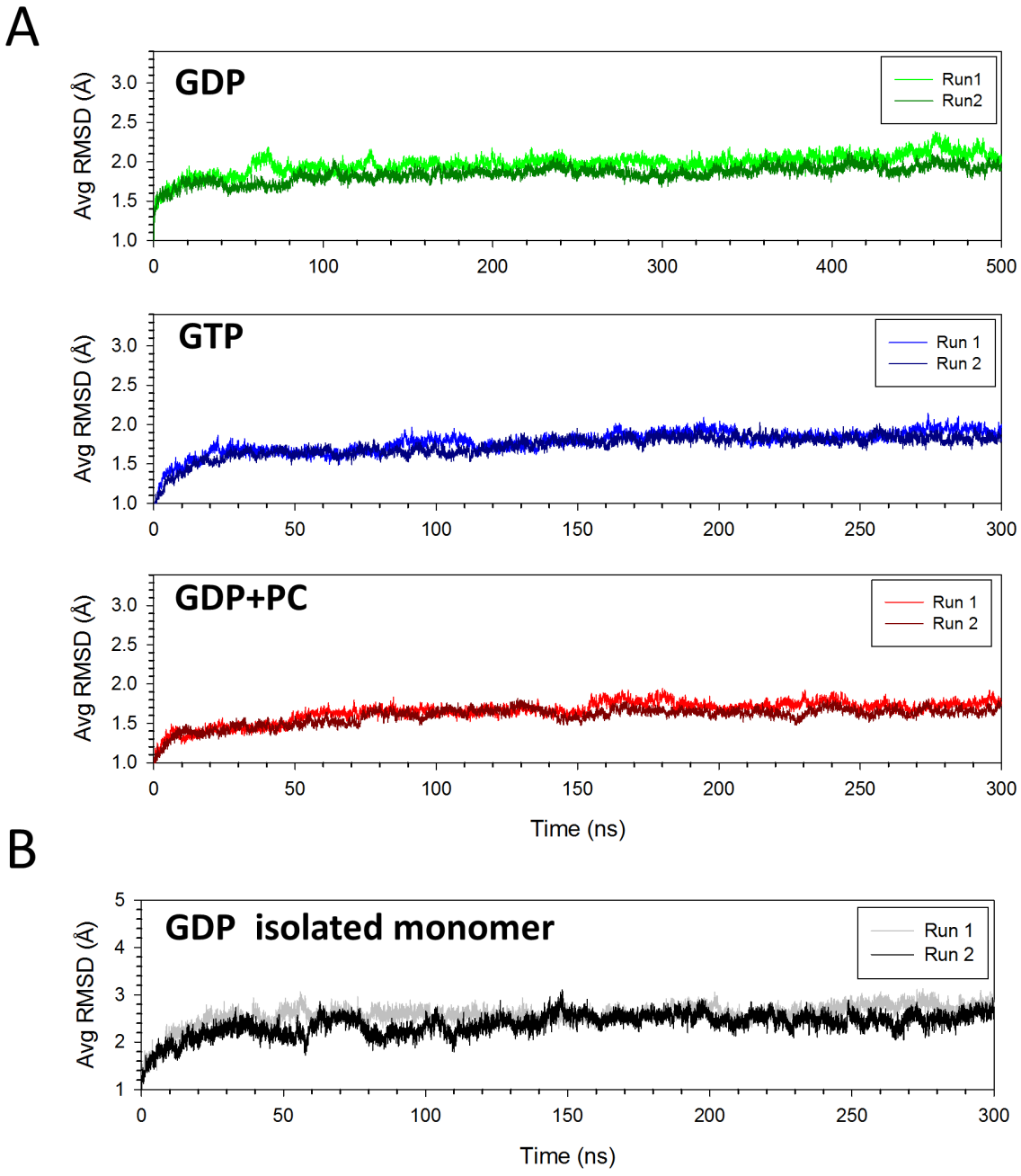

Figure S1. RMSD evaluated along the trajectories. (A) Average RMSD of the FtsZ monomers within the corresponding filaments along trajectories. The structures of the two end monomers have been excluded to avoid border effects, and two runs are plotted per case. (B) Average RMSD for the isolated GDP FtsZ monomer. In all the cases, the RMSD was computed considering backbone atoms using g_rmsd from GROMACS tools.

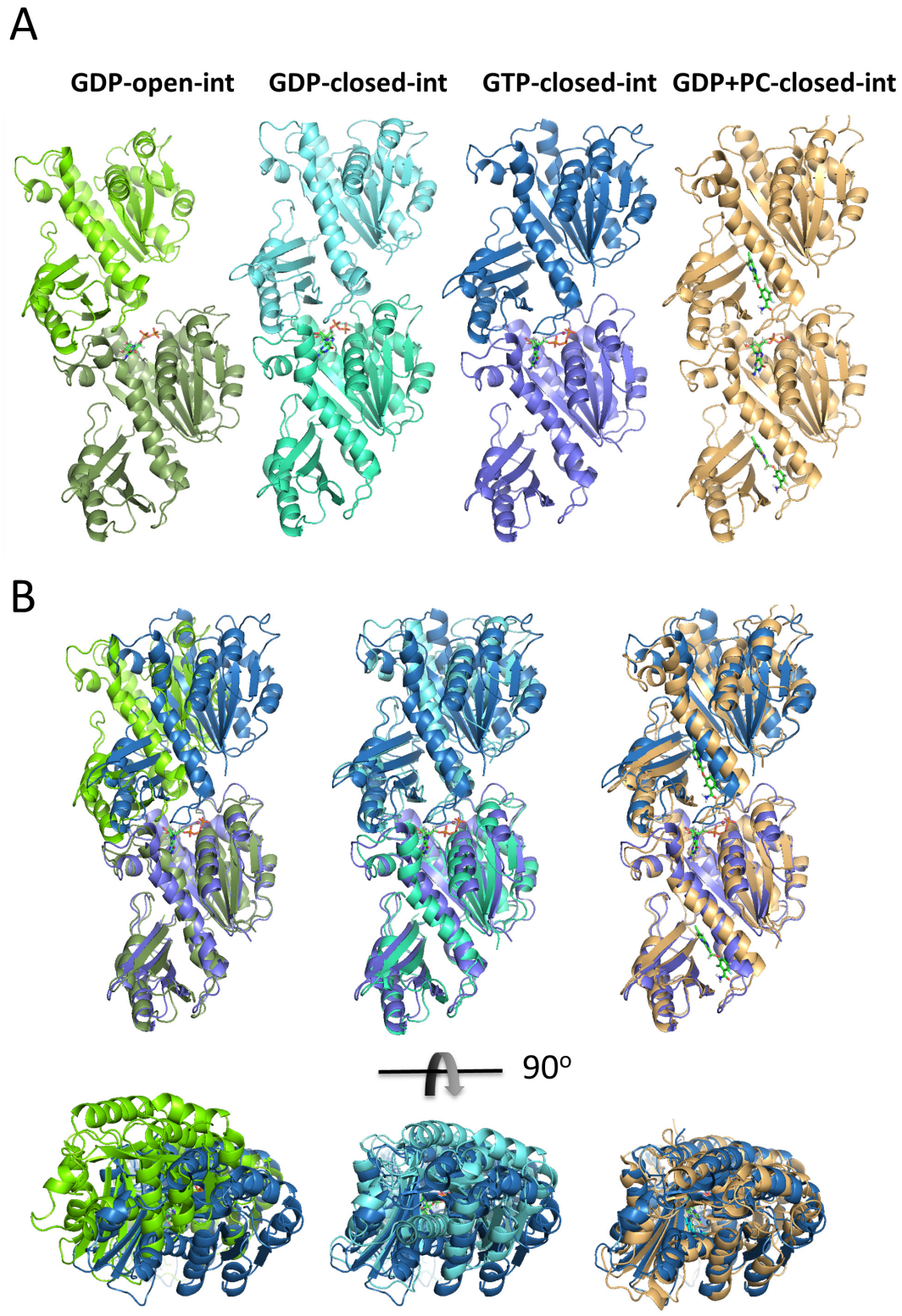

Figure S2. A. Illustrative dimer structures corresponding to GDP-open (green), GDP-closed (cyan), GTP (blue) and PC (wheat) monomer-to-monomer interfaces. B. Alignment of the GDP-open, GDP-closed and PC dimers with the GTP dimer.

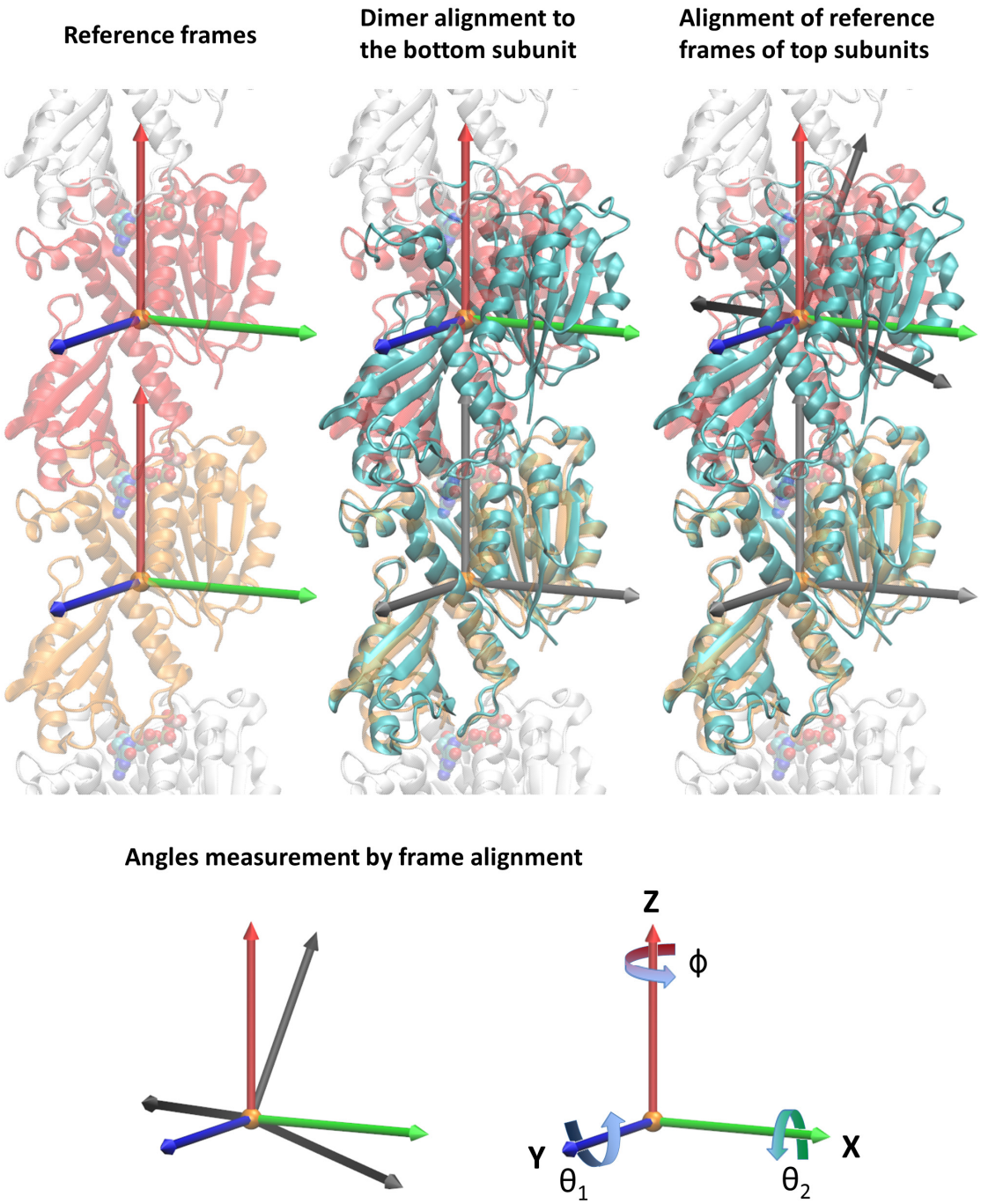

Figure S3. Definitions of bending and twisting angles. The relative orientation of each pair of monomers was monitored throughout the final 100 ns of the trajectories following a described methodology (1, 2). In brief, the coordinate frame was defined by aligning the z axis along the monomers' centers of mass, fixing the x axis along the direction of bending and defining an orthogonal y axis. For comparative proposes, the main bending angle $\theta_1$was set to lie in the maximal bending direction of the GTP filament. Rotations around the axes of the coordinate frame defined the bending and twisting angles that could be individually tracked for each monomer-monomer pair in the filaments, as depicted. To measure the angles, two consecutive monomers were first aligned with respect to the straight reference by superposing the bottom monomers. The corresponding bending angles are tracked by calculating the sequential rotations to align the coordinate reference frames of the top monomers. The bending angles θ_1 and θ_2 were defined by rotations around the Y axis (blue) and the X axis (green), respectively and the twist (Φ) was defined by the rotation around the Z axis (red). Note that this view is roughly equivalent to tubulin viewed from the inside of a microtubule.

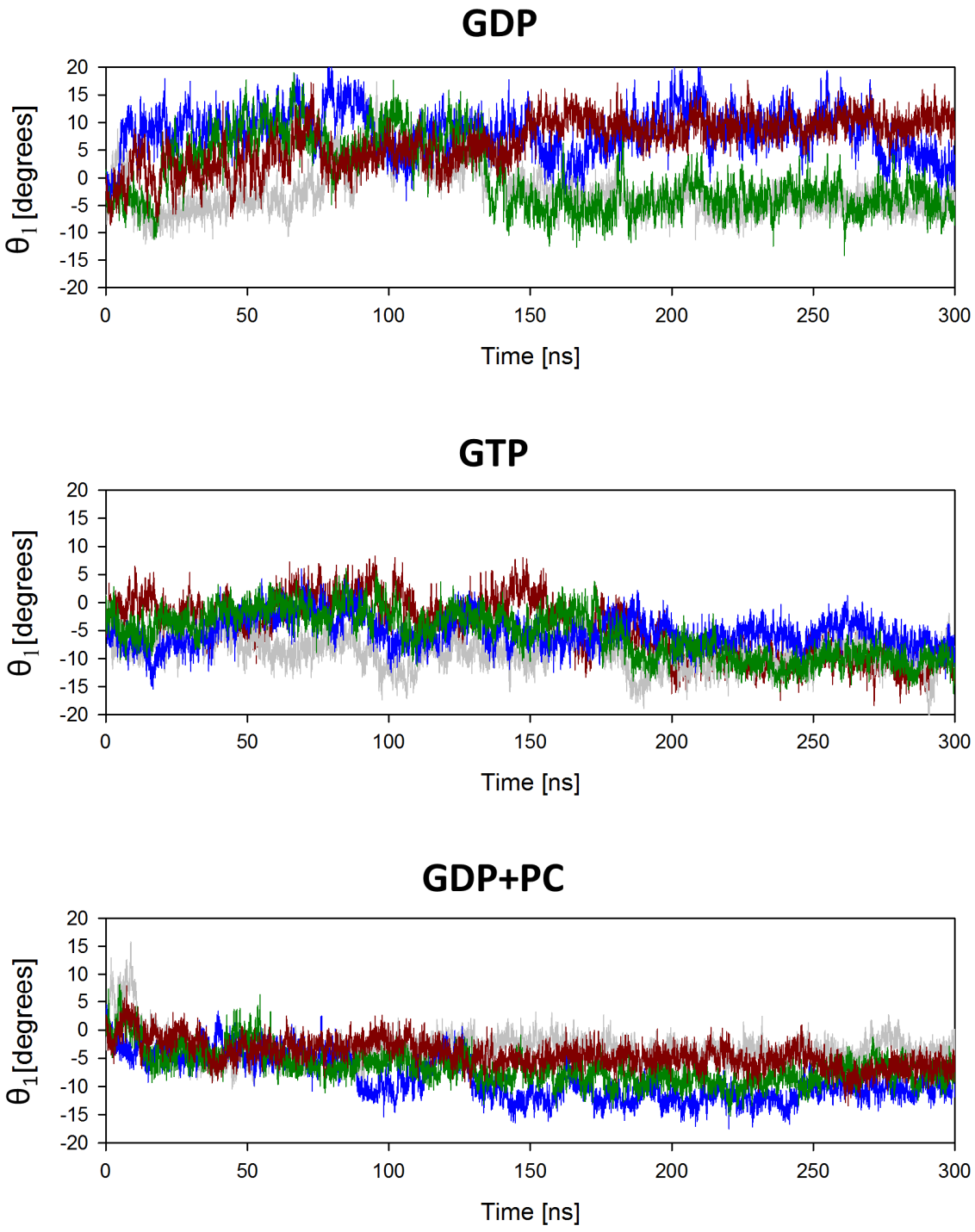

Figure S4. Time evolution of the main bending angle θ_1 for the four central interfaces of filament calculated as described in Fig. S3. Notice that the GDP-filament converges to heterogeneous filament formed by open (~6 degrees) and closed (~-6 degrees) interfaces. In contrast, the monomer association remains closed during all the simulations for GTP and GDP-bound filaments

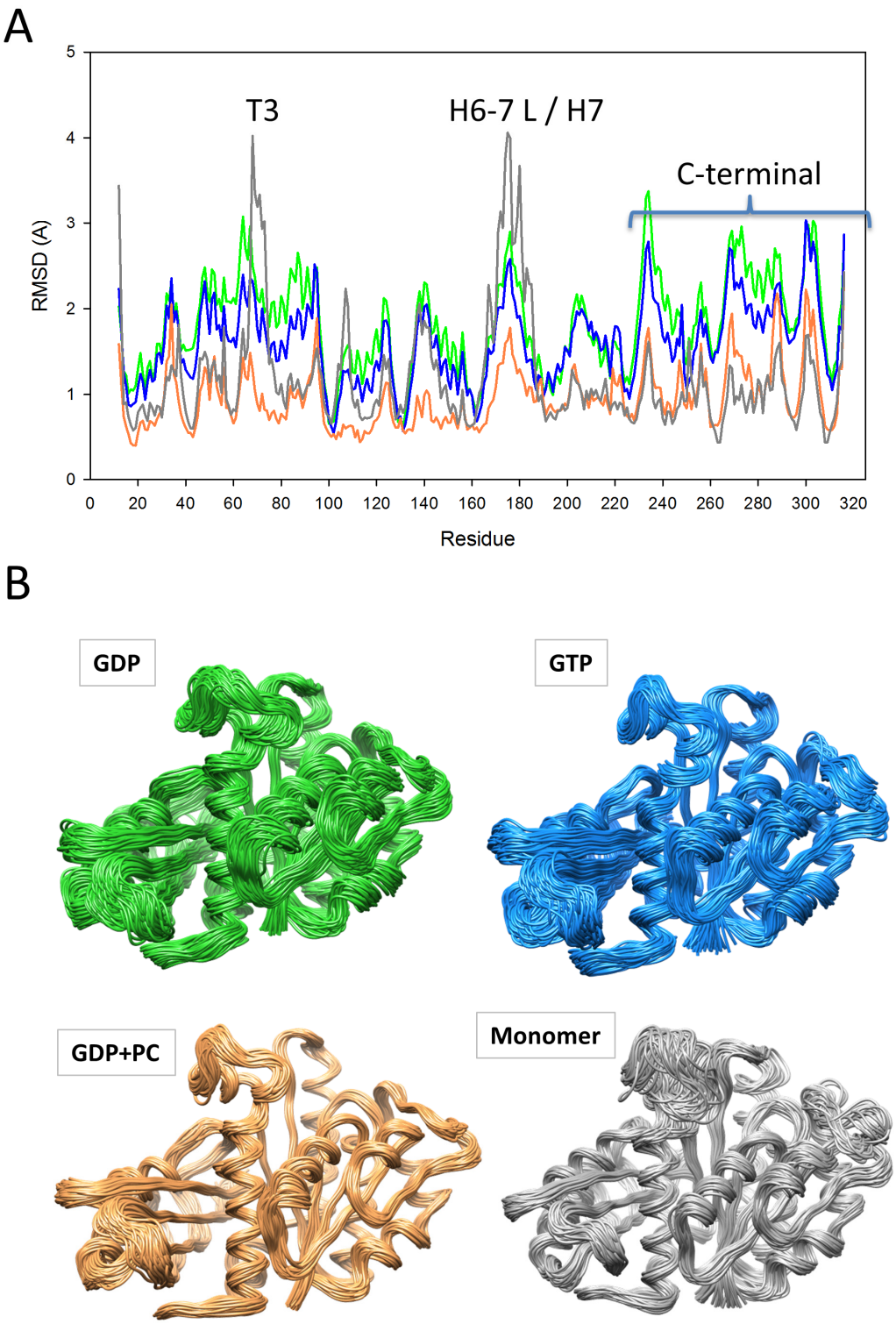

Figure S5. Average monomer conformations from the final 100 ns of the trajectories were aligned via a maximum-likelihood superimposition criterion using THESEUS (3) for the GDP filament (green), the GTP filament (blue), the PC filament (wheat) and an isolated GDP FtsZ monomer (gray). (A) Average RMSD per residue obtained from the superimposition. (B) Corresponding ensemble overlaps.

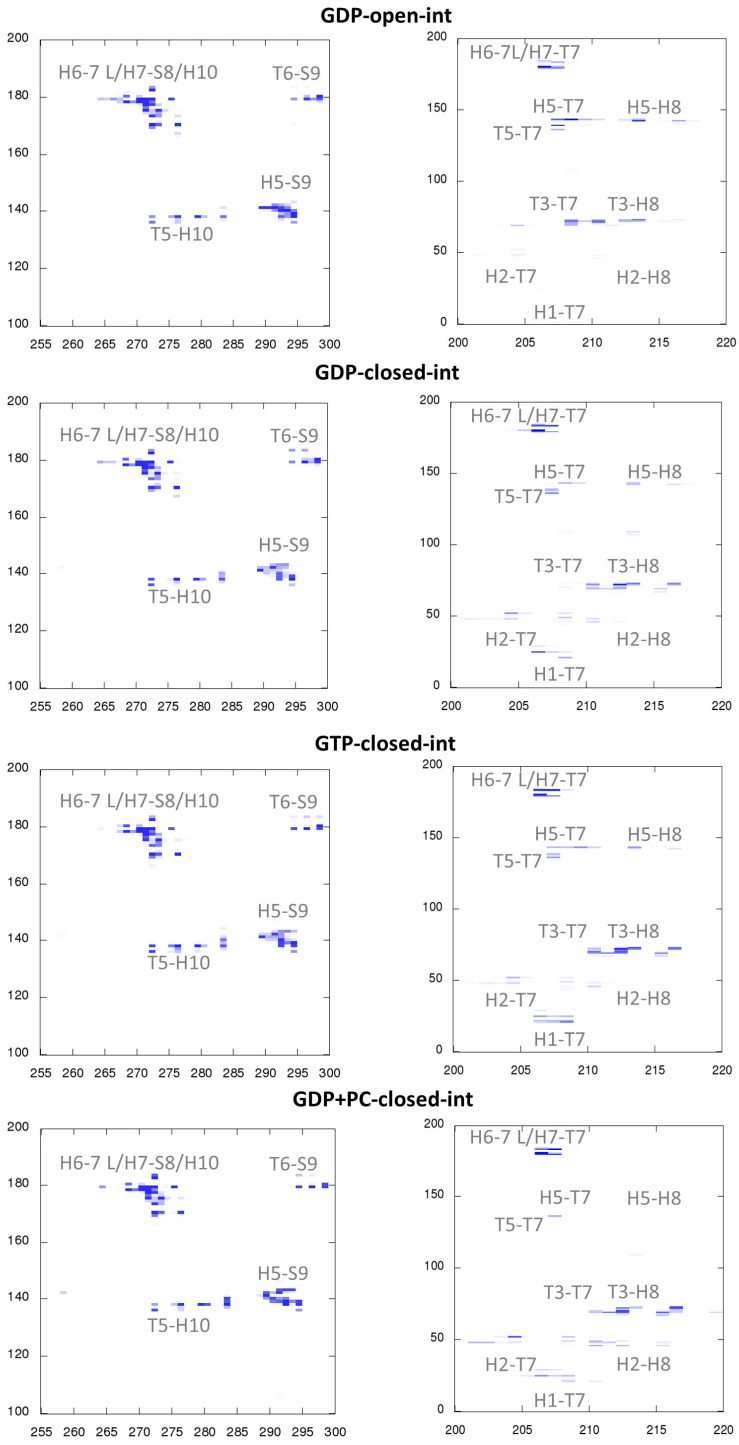

Figure S6. Contact plots of the monomer-monomer interfaces. Two residues were considered to be in contact if they had at least one pair of atoms separated by less than 4 Å. Contacts were calculated for the four central monomer interfaces throughout the final 100 ns of the simulations. The numbers in the axes are residue positions. The intensity of each band reflects the percentage of simulation time during which the contact was present. Dark blue regions correspond to contacts that were present throughout the entire simulation time. The relative differences between GDP and GTP contact patterns are detailed in the main text. In comparison to the simulations with bound GDP, the presence of PC stabilized the contacts of the top monomer's T7 loop with the bottom monomer's H2 and H1 helices and those

formed by H2-H8, and impeded the contacts of bottom H5 helix observed with other filaments. As shown by the crystal structure (4-6), the benzamide moiety makes the major contribution to the binding. During our simulations, the amide group formed stable H-bonds with Val207 (T7) and Asn263 (H8) and, in a more transient fashion, with Gly205 and Leu209. The thiazolopyridine part of the ligand interacted with the H7 helix (residues Gly193, Gly192 and Glu196) and with the C-terminal domain (residues Met226 and Ile228). Interestingly, the presence of PC impeded the contacts with the H5 helix disrupting the stable H-bonds of Asp-213 with Lys142 and Arg143 that were observed in the other filaments. By contrast, more stable contacts of the H2 helix with the T7 loop and the H8 helix were present; for example, the binding of Asp210 (T7) to the T3-loop glycine cluster observed in other cases was replaced by an interaction with Gln48 (H2).

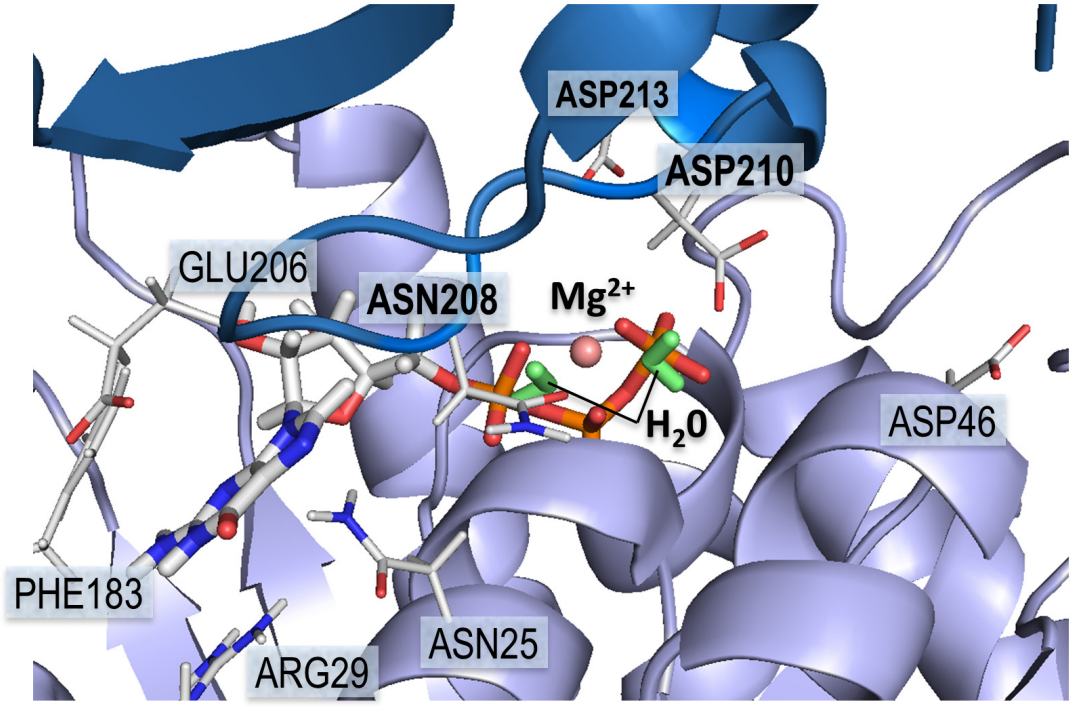

Figure S7. Detailed view of the GTP-filament interface. Among the elements of the Mg^{2+} coordination shell, the strongest interactions corresponded to the Asn208 from the T7 loop and to the β and γ phosphates (orange). The magnesium interactions held the binding pocket closed and stabilized the GTP nucleotide in a position suitable for hydrolysis. In this case, the carbonyl group of Asp210 is located at the correct hydrogen-bonding distance to polarize one of the water molecules (green) coordinated with the magnesium (pink).

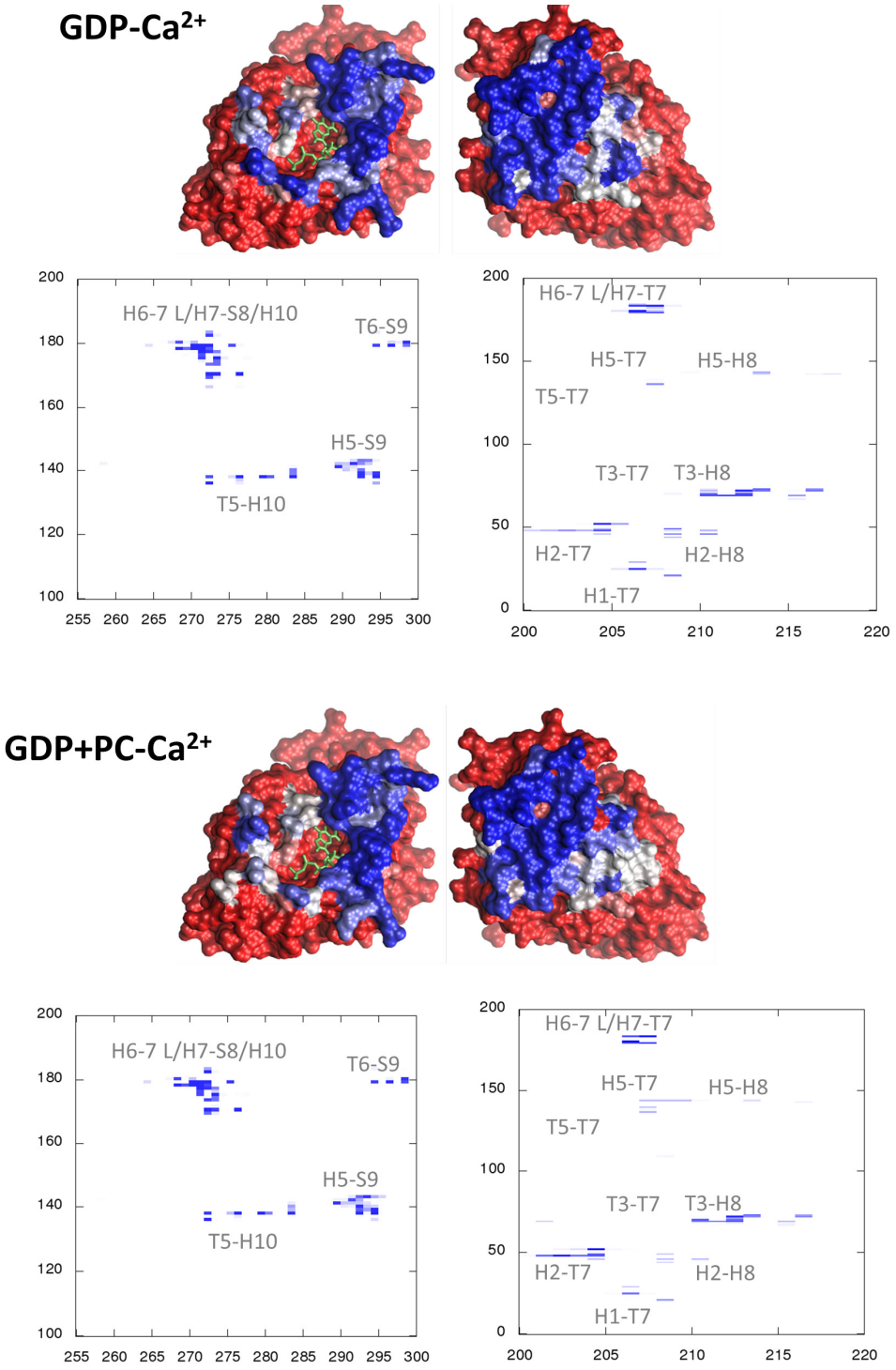

Figure S8. Contact surfaces and interface contact plots of the monomer-monomer interface for FtsZ filament simulations with a bound Ca^{2+} ion (see Fig. 3 and SI Fig. S6 for corresponding results without Ca^{2+}). In comparison to the simulations without calcium, there was an apparent increase in the inter-monomer contact near H2. As observed in the crystal structure, Ca^{2+} formed a coordination center with two water molecules inside the T7 loop. In our simulations, we found that the carbonyl groups of Leu200, Val203, Ser204, Asn280 and Asp210 were all located at compatible coordinating distances, but the Ca^{2+} ion interacted more closely with the latter two residues. Other important interactions were detected with either Asp46 or Gln48 at the H2 helix of the bottom subunit.

Movies

FtsZ_Movie 1. MD simulation trajectories of GDP-, GTP- and PC-bound filaments.

FtsZ_Movie 2. Animation of the transition among GTP, GDP-closed and GDP-open states. A feasible pathway was generated among the illustrative dimers extracted from the corresponding MD filament simulations. As in Fig. 1, the blue color represents GTP, cyan represents GDP-closed dimers, and green represents GDP-open dimers. The transitions were obtained using the normal-mode analysis in internal coordinates suite iMOD (7). Notice that the orientations of movie 1 (Fig. 1A) and movie 2 (Fig. 1B) are related by a rotation of 45 degrees around the axis of the filament.

FtsZ_Movie 3. MD simulation of the activation switch. The conformational change observed with a single SaFtsZ monomer during the transition from the open-cleft to the closed-cleft conformations. The movie includes the first 35 ns of the simulation.

Supporting References

1. Hsin J, Gopinathan A, & Huang KC (2012) Nucleotide-dependent conformations of FtsZ dimers and force generation observed through molecular dynamics simulations. *Proc Natl Acad Sci U S A* 109(24):9432-9437.
2. Grafmuller A & Voth GA (2011) Intrinsic bending of microtubule protofilaments. *Structure* 19(3):409-417.
3. Theobald DL & Wuttke DS (2008) Accurate structural correlations from maximum likelihood superpositions. *PLoS Comput Biol* 4(2):e43.
4. Matsui T, *et al.* (2012) Structural reorganization of the bacterial cell-division protein FtsZ from Staphylococcus aureus. *Acta Crystallogr Sect. D Biol Crystallogr* 68(9):1175-1188.
5. Tan CM, *et al.* (2012) Restoring methicillin-resistant Staphylococcus aureus susceptibility to β-lactam antibiotics. *Sci Transl Med* 4(126):126ra135.
6. Elsen NL, *et al.* (2012) Mechanism of action of the cell-division inhibitor PC190723: modulation of FtsZ assembly cooperativity. *J Am Chem Soc* 134(30):12342-12345.
7. Lopez-Blanco JR, Garzon JI, & Chacon P (2011) iMod: multipurpose normal mode analysis in internal coordinates. *Bioinformatics* 27(20):2843-2850.